AFRL-AFOSR-VA-TR-2020-0006

Study of Next Generation Propulsion Systems Using Advanced High Speed Laser Diagnostics

Tonghun Lee
UNIVERSITY OF ILLINOIS

11/01/2019
Final Report

Air Force Research Laboratory
AF Office Of Scientific Research (AFOSR)/ RTA1
Arlington, Virginia 22203
Air Force Materiel Command

REPORT DOCUMENTATION PAGE

Form Approved
OMB No. 0704-0188

1. REPORT DATE *(DD-MM-YYYY)* 31-10-2019	**2. REPORT TYPE** Final	**3. DATES COVERED** *(From - To)* 09/30/2014-09/29/2019

4. TITLE AND SUBTITLE
PECASE- Study of Next Generation Propulsion Systems Using Advanced High Speed Laser

5a. CONTRACT NUMBER

5b. GRANT NUMBER
FA9550-14-1-0343

5c. PROGRAM ELEMENT NUMBER

6. AUTHOR(S)
Dr. Tonghun Lee

5d. PROJECT NUMBER

5e. TASK NUMBER

5f. WORK UNIT NUMBER

7. PERFORMING ORGANIZATION NAME(S) AND ADDRESS(ES)
University of Illinois
506 S Wright St, 364 Henry Admin Bldg
Urbana, IL 61801-3620

8. PERFORMING ORGANIZATION REPORT NUMBER

9. SPONSORING/MONITORING AGENCY NAME(S) AND ADDRESS(ES)
USAF, AFRL
AF Office of Scientific Research
875 North Randolph Street, Rm 3112
Arlington, VA 22203-1954

10. SPONSOR/MONITOR'S ACRONYM(S)

11. SPONSOR/MONITOR'S REPORT NUMBER(S)

12. DISTRIBUTION/AVAILABILITY STATEMENT
Approved for public release; distribution is limited

13. SUPPLEMENTARY NOTES
none

14. ABSTRACT

This study summarizes an effort to understand the multi-scale and multi-physics phenomena in supersonic and hypersonic reactive environments relevant to the Air Force, and the development of advanced diagnostics to support this vision. Significant achievements were made in four separate, but synergistic areas. First an arc-heated hypersonic wind tunnel at the University of Illinois (ACT-II) was developed for experimental research in supersonic combustion. Second, a novel 2D laser diagnostics for imaging of turbulent flames using the CH C-X transition has been developed and demonstrated with high SNR using low laser energies. Third, a novel nanosecond-gated laser-induced breakdown spectroscopy (nano-LIBS) was developed to be a practical and effective technique for quantitative gas property measurements in supersonic reactive environments. Finally, studies of combustion-induced unstart phenomena and flame stabilization in axisymmetric scramjet models were conducted in the ACT-II facility using advanced high speed measurement techniques.

15. SUBJECT TERMS
Supersonic Combustion, High Speed Laser Diagnostics, Hypersonic Propulsion, Scramjet Unstart

16. SECURITY CLASSIFICATION OF:			**17. LIMITATION OF ABSTRACT**	**18. NUMBER OF PAGES**	**19a. NAME OF RESPONSIBLE PERSON**
a. REPORT	**b. ABSTRACT**	**c. THIS PAGE**			Chiping Li
U	U	U	UU		**19b. TELEPHONE NUMBER** *(Include area code)* 703-481-6930

Reset

Standard Form 298 (Rev. 8/98)
Prescribed by ANSI Std. Z39.18

INSTRUCTIONS FOR COMPLETING SF 298

1. REPORT DATE. Full publication date, including day, month, if available. Must cite at least the year and be Year 2000 compliant, e.g. 30-06-1998; xx-06-1998; xx-xx-1998.

2. REPORT TYPE. State the type of report, such as final, technical, interim, memorandum, master's thesis, progress, quarterly, research, special, group study, etc.

3. DATES COVERED. Indicate the time during which the work was performed and the report was written, e.g., Jun 1997 - Jun 1998; 1-10 Jun 1996; May - Nov 1998; Nov 1998.

4. TITLE. Enter title and subtitle with volume number and part number, if applicable. On classified documents, enter the title classification in parentheses.

5a. CONTRACT NUMBER. Enter all contract numbers as they appear in the report, e.g. F33615-86-C-5169.

5b. GRANT NUMBER. Enter all grant numbers as they appear in the report, e.g. AFOSR-82-1234.

5c. PROGRAM ELEMENT NUMBER. Enter all program element numbers as they appear in the report, e.g. 61101A.

5d. PROJECT NUMBER. Enter all project numbers as they appear in the report, e.g. 1F665702D1257; ILIR.

5e. TASK NUMBER. Enter all task numbers as they appear in the report, e.g. 05; RF0330201; T4112.

5f. WORK UNIT NUMBER. Enter all work unit numbers as they appear in the report, e.g. 001; AFAPL30480105.

6. AUTHOR(S). Enter name(s) of person(s) responsible for writing the report, performing the research, or credited with the content of the report. The form of entry is the last name, first name, middle initial, and additional qualifiers separated by commas, e.g. Smith, Richard, J, Jr.

7. PERFORMING ORGANIZATION NAME(S) AND ADDRESS(ES). Self-explanatory.

8. PERFORMING ORGANIZATION REPORT NUMBER. Enter all unique alphanumeric report numbers assigned by the performing organization, e.g. BRL-1234; AFWL-TR-85-4017-Vol-21-PT-2.

9. SPONSORING/MONITORING AGENCY NAME(S) AND ADDRESS(ES). Enter the name and address of the organization(s) financially responsible for and monitoring the work.

10. SPONSOR/MONITOR'S ACRONYM(S). Enter, if available, e.g. BRL, ARDEC, NADC.

11. SPONSOR/MONITOR'S REPORT NUMBER(S). Enter report number as assigned by the sponsoring/ monitoring agency, if available, e.g. BRL-TR-829; -215.

12. DISTRIBUTION/AVAILABILITY STATEMENT. Use agency-mandated availability statements to indicate the public availability or distribution limitations of the report. If additional limitations/ restrictions or special markings are indicated, follow agency authorization procedures, e.g. RD/FRD, PROPIN, ITAR, etc. Include copyright information.

13. SUPPLEMENTARY NOTES. Enter information not included elsewhere such as: prepared in cooperation with; translation of; report supersedes; old edition number, etc.

14. ABSTRACT. A brief (approximately 200 words) factual summary of the most significant information.

15. SUBJECT TERMS. Key words or phrases identifying major concepts in the report.

16. SECURITY CLASSIFICATION. Enter security classification in accordance with security classification regulations, e.g. U, C, S, etc. If this form contains classified information, stamp classification level on the top and bottom of this page.

17. LIMITATION OF ABSTRACT. This block must be completed to assign a distribution limitation to the abstract. Enter UU (Unclassified Unlimited) or SAR (Same as Report). An entry in this block is necessary if the abstract is to be limited.

FINAL REPORT

PECASE: STUDY OF NEXT GENERATION PROPULSION SYSTEMS USING ADVANCED HIGH SPEED LASER DIAGNOSTICS

AFOSR Grant Number: FA9550-14-1-0343

October 2019

Tonghun Lee
Department of Mechanical Science & Engineering
University of Illinois at Urbana-Champaign
1206 W. Green Street
Urbana, IL 61801
tonghun@illinois.edu
(517)290-8005

1. ABSTRACT

This final report summarizes an effort to understand the multi-scale and multi-physics phenomena in highly turbulent flames over a wide range of supersonic and hypersonic conditions relevant to Air Force interests, and the development of advanced diagnostics that will enable this vision. The goal is to study well-defined generic hypersonic conditions that will provide insight into the key physicochemical phenomena at practical high-speed flight conditions. Significant achievements were made in four separate, but synergistic areas outlined in the proposal.

The arc-heated hypersonic wind tunnel at the University of Illinois (ACT-II) has been developed for experimental research in supersonic combustion and laser diagnostics. The novel ground testing facility can provide high-enthalpy flow conditions replicating the hypersonic flight at Mach 4.5-9 at an altitude of above 35 km. The new facility has proven to be a flexible platform for studies of flow dynamics, supersonic flame ignition, stabilization, and propagation phenomena, and applications of the state-of-art laser diagnostic technologies.

The latest laser diagnostic on turbulent flames using a CH C-X transition strategy has been developed and applied in a number of laboratory combustors. This laser transition is about two orders of magnitude more efficient than conventional transitions for CH, enabling high speed imaging at framerates exceeding 10 kHz. In addition, CH C-X imaging can employ satellite transition excitation and customized sharp filters to cut off the laser scattering, enabling the application of multiple scattering-based flame diagnostics techniques simultaneously, such as CH flame front imaging and high-speed PIV with flow seeding.

In addition to CH C-X PLIF, novel nanosecond-gated laser-induced breakdown spectroscopy (nano-LIBS) has shown to be a practical and effective technique for quantitative gas property measurements in high-speed combustion with minimal system complexity. In the AFRL RC-19 facility at Wright Patterson Air Force Base, fuel concentration and gas density were mapped throughout the flame holder cavity for various inlet shock impingement conditions using this technique. Through the construction of an intensive spectrum database and the development of the direct spectrum matching procedure, fuel concentration and gas density were mapped throughout the flame holder cavity of a model scramjet operating at Mach 3 and with different geometries. the introduction of fuel surrogates (CO_2), allowed to better characterize fuel concentrations and statistics in non-combusting case.

Experimental investigations conducted in the ACT-II facility consist of combustion-induced flow choking and unstart phenomena with constant-area and diverging combustors, the pseudo shock dynamics in the scramjet during dual-mode operation, and incipient unstart processes. In these experimental investigations, the axisymmetric scramjet model has been used to study the generic physicochemical process without corner flow effects encountered in the rectangular combustor geometries. The hydroxyl planar laser induced fluorescence, Rayleigh scattering, high-frequency pressure measurement, pitot probe and heat flux measurements have been used to resolve the flow and flame dynamics.

2. INTRODUCTION

Hypersonic vehicles provide the potential for the fastest long-range flight capability in applications for national security, space exploration and civil transportation. The air-breathing supersonic combustion ramjet (scramjet) engine is essential for developing hypersonic vehicles since it provides the highest specific impulse at hypersonic flight conditions; the source of this efficiency can be attributed to the use of oxidant from atmospheric air in the supersonic combustion processes. The development of scramjet propulsion technology mainly focuses on i) advanced weapon systems for global strike and reconnaissance, ii) affordable and reusable space access systems for space exploration, and iii) the high-speed long range aircrafts for commercial transportation around the globe. Scramjets, along withpulse detonation engines and next-generation gas turbine engines will be key components of high-speed transportation for both military and civilian applications in the future.

The combustion process occurring in these engines involves high-speed, highly turbulent reacting flow conditions which are beyond our current quantitative understanding of the physicochemical phenomena. Efforts implemented in this research will provide a transformative advancement in our understanding of the high-speed turbulent combustion and flame dynamics over a wide range of realistic operation conditions. This understanding will be essential for the development of next generation propulsion systems. The United States Air Force devotes significant effort in developing the X-51 scramjet and the fundamental research on the high-speed turbulent reacting flows. Studies shown in this report further extend those endeavors and will provide a foundational scientific knowledge base on turbulent combustion based on the state-of-art diagnostics.

Development of next generation propulsion systems is fraught with a vast range of technical challenges. The scramjet, for example, while offereing the benefits of a simple design, reduced weight, low drag and high combustion efficiency, also faces significant engineering challenges in flow control and combustion stability due to the supersonic airflow through the entire engine and resulting high Reynolds number regimes [Heiser,Curran]. In case of hypersonic scramjet engines, upstream influences do not propagate within the free stream of the combustion chamber. As a result, throttle control at the entrance of the thrust nozzle is ineffective and a block of gas entering the combustion chamber must mix sufficiently with the fuel and undergo combustion before the burned gas is expanded through the nozzle. This limits the temperature and pressure ranges which allow efficient fuel-air mixing and stable combustion to occur. Operation outside this range can result in various acoustic problems, oscillations and instabilities in the combustion due to the mutual coupling between the unsteady heat release and local flow fluctuations in the flame zone [Li]. The cause for these challenges mainly stems from our inability to fully understand the basic turbulent dynamics under the relevant flow conditions. Therefore, significant experimental and numerical research is required to optimize the design of practical next generation propulsion systems.

This study has been dedicated to understanding the multi-scale and multi-physics phenomena in highly turbulent flames over a wide range of supersonic and hypersonic conditions and the development of advanced diagnostics that will enable this vision. The goal is to study well-defined generic conditions that will ***provide insight into the key physicochemical phenomena in practical flight conditions,*** resulting in profound and transformative evolution in our understanding of turbulent flames and the key rate limiting physics. The study is highly collaborative in nature, utilizing partnerships with the Aerospace Propulsion Division at Wright Patterson Air Force Base (WPAFB) for in-situ measurements in supersonic wind tunnels for cavity flame holding, and other University collaborations for probing turbulent flame dynamics.

3. BACKGROUND (Diagnostics)

The last decade has seen transformative advancements in high speed imaging of key chemical radicals in combustion. Advances in pulse burst technology has opened the door for generating bursts of high powered pulse trains at extremely high repetition rates [Fuest,Gabet,Slipchenko]. On the continuous side of the measurement spectrum, we have also benefitted from dramatic advances in technology in both high-speed tunable lasers (*i.e.*, Sirah high-repetition dye lasers) and intensifiers (*i.e.*, Lavision two stage HS-IRO, Hadland kHz Intensifier), providing an opportunity to selectively tune excitation wavelength and collect LIF at > kHz rates with sufficient signal, sustained operation, and a high level of flexibility.

Some of the most advanced demonstrations of this technology were made by Dr. Lee in collaboration with Dr. Campbell Carter of AFRL. The state of the art at this writing is being able to routinely apply OH-PLIF imaging at 50 kHz framerates with SNR in excess of 25 as shown in **Figure 1** [Hammack], demonstrated by the PI in 2013. Here, a transient arc DC plasma stabilized flame was used for the OH PLIF measurements. A high speed dye laser was pumped by a 50-kHz Nd:YAG laser systems at 532 nm. In order to achieve these results, the dye laser system was re-designed to handle the thermal loading on the optics and amplifier cells. In particular, a two-crystal doubling unit was implemented to handle the high flux of energy going through the system. As a result, the new system was able to yield conversion efficiencies rivaling that of conventional low repetition systems.

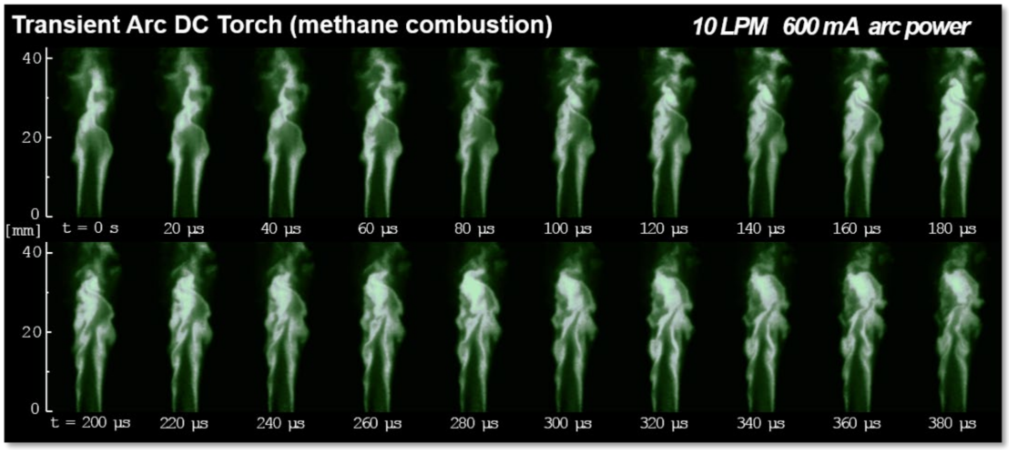

Figure 1. Continuous 50 kHz OH PLIF in a transient arc DC torch [Hammack]. The OH concentrations are comparable to that found in a premixed laminar flame.

In addition to the evolution of high-speed laser systems, two significant advances in imaging of flame dynamics were made by the PI and Dr. Carter (AFRL) in the past two years that hold promise to revolutionize the diagnostics of turbulent flames. The first technology was the introduction of a new transition in imaging CH radicals in flames. Dr.'s Lee and Carter have recently demonstrated that a new transition of the CH radical (C–X transition) will enable PLIF images to be obtained with up to two orders of increased efficiency, which translates to detailed images which can be extended into the kHz regime [Carter]. The second advancment was made in single point detection of thermodynamic conditions using a novel nanosecond laser induced breakdown spectroscopy method, which has in the past two years been demonstrated to yield remarkable results in the TC-19 supersonic combustion tunnel at Wright Patterson Air Force Base.

4. DEVELOPMENT OF THE ACT-II FACILITY

A new pulsed, arc-heated, hypersonic combustion test rig has been designed and built at the University of Illinois. The new facility is an improved version of the hypersonic test rig ACT-I. The aim of ACT-II is to provide an experimental test-bench for the study of turbulent combustion in supersonic regime and the development of new laser diagnostic techniques being able to provide a quantitative characterization of the flow physics involved in the combustion process. The driving factors of the design of the new facility were:

- **Enhanced Arc Stability:** ACT-II employs improved power supply and arc generator for more stable arc generation over a wide range temperature, pressures, and flow conditions.
- **Flexibility:** ACT-II enables flexible adjustment of the flow properties (stagnation conditions, Mach number, air composition, etc.) and the combustion conditions (equivalence ratio, compression ratio, etc.).
- **Scramjet Geometry:** The ACT-II can accommodate a range of scramjet geometries. Initially, ACT-II can be fitted with a circular scramjet configuration which eliminates the corner effects with square geometry.

Optical Access: The design of ACT-II is strongly oriented to optimize laser diagnostics for close-up imaging of the combustion dynamics.

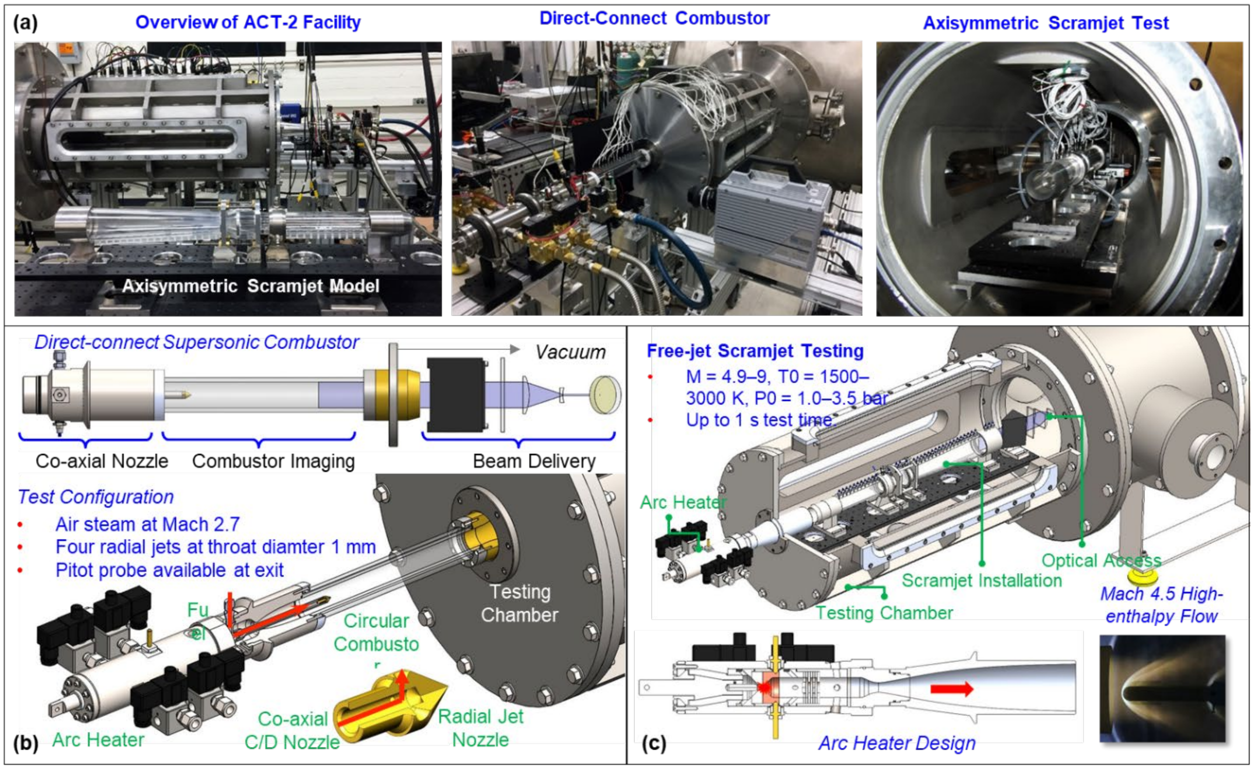

Figure 2. (a) Overview of the ACT-II facility, (b) direct-connect supersonic combustor, (c) free-jet scramjet testing.

Figure 2 shows an overview picture of ACT-II. ACT-II is a pulsed, high-enthalpy (up to 4.5 MJ/kg), blowdown wind tunnel specifically designed for supersonic combustion research. The facility consists of two high-pressure tanks, where the working gases (nitrogen and oxygen) are initially stored, a hot-gas generator (arc-jet type), a converging-diverging (C-D) nozzle, a test-section/combustor and a vacuum tank where the gas is exhausted. The arc-heater of ACT-II has a coaxial electrodes configuration with a cylindrical cathode (lanthanated tungsten) and an annular anode (TZM alloy), separated by a ceramic constrictor.

A typical DC voltage of 550-600 V is initially applied between the electrodes, and when the gas is injected, an electric discharge is initiated by voltage breakdown. In normal operations the arc is ignited in argon gas and successively transitioned to nitrogen. Oxygen is injected downstream of the anode and mixed with the heated nitrogen using a set of ceramic screens. This injection method reduces the erosion of the electrodes (and the consequent contamination of the flow) by limiting the formation of atomic oxygen in the arc chamber.

The mixture, equivalent in composition to air (N_2 and O_2), reaches thermodynamic equilibrium flowing at low speed through a plenum chamber and then is expanded to supersonic speed by the C/D nozzle. The nozzle can be directly connected to a combustor (direct-connect mode) or attached to a test-section to operate the facility in free-jet mode. Arc voltage and current, plenum pressure and mass flow rates of freestream and fuel are monitored in real time during each tunnel run. Depending on the flow conditions, the typical test time ranges between 500 and 1000 ms.

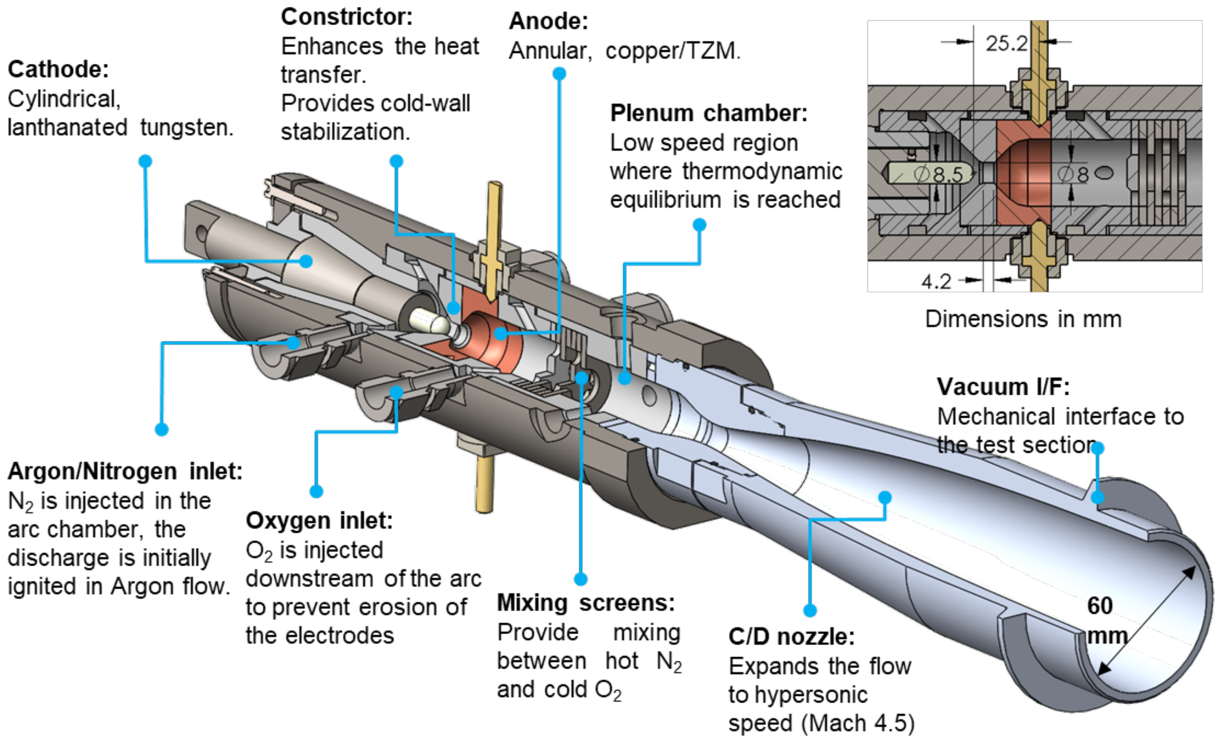

Figure 3. Cross section of the arc-heater.

The working gas (a mixture of nitrogen and oxygen) is initially stored in reservoirs and is introduced into the arc-heater by means of a series of fast opening solenoid valves. The gas is heated by the electric discharge and is expanded to hypersonic velocity through a C/D nozzle. The exit of the nozzle is connected to a vacuum chamber (total volume ~4 m^3) in order to keep the flow in under-expanded conditions for the whole duration of the test. The hypersonic flow enters the scramjet model where it is compressed by a train of oblique shocks and is mixed with the fuel injected from a supersonic nozzle in the side wall of the combustor. The ignition is triggered by the temperature of the mixture, which is above the value for auto-ignition of the fuel.

The arc-heater (**Figure 3**) has a coaxial electrodes configuration with a cylindrical tungsten cathode and an annular copper anode. A DC voltage (typically 550 - 700 V) is applied between the electrodes and when the gas is injected into the arc chamber, an electric discharge is initiated by voltage breakdown. Between anode and cathode, the flow is forced to pass through a ceramic-made restricted section (constrictor) that enhances the thermal exchange between the working gas and the electric arc. The constrictor also promotes the stabilization of the plasma column by cold wall effect [Pfender]. In normal operating mode, only nitrogen is injected into the arc-chamber and is successively mixed with cold oxygen to yield a flow with the proper composition and temperature. This solution helps to extend the operational life of the electrodes, avoiding a direct contact with the atomic oxygen produced by O_2 dissociation and also limits the production of NO_X particles that, being extremely reactive, may alter the natural combustion dynamics [Bowman, Guo].

After oxygen injection, the mixture passes through a set of screens provided with holes of different size and arranged in different pattern in order to provide mixing and improve uniformity of temperature and compositions. By changing the geometry of these screens is also possible to control, to a certain extent, the turbulence level in the supersonic freestream. This allows for the investigation of the effects of turbulence on combustion. Downstream of the screens, the gas flows at low speed through a constant area duct (plenum or settling chamber) with a length sufficient to guarantee a residence time long enough to reach a condition of thermodynamic equilibrium. The pressure in the plenum chamber, which can be considered as the total pressure of the flow, is measured by means of a Kulite piezoresistive pressure transducer with an accuracy higher than 1%. A total of four access ports are available in the plenum chamber for a complete characterization of the stagnation conditions of the gas. Downstream of the plenum chamber the gas is expanded through a C/D nozzle up to the design Mach number.

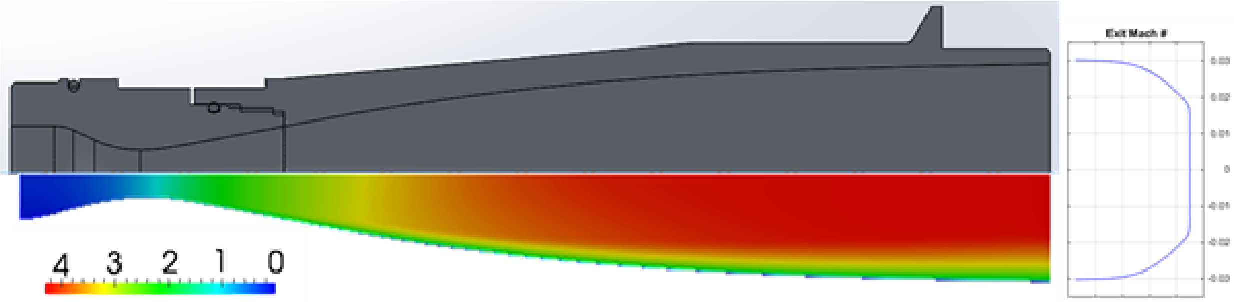

Figure 4. Mach 4.5 nozzle cross section with the numerical simulation of the Mach number.

A Mach 4.5 contoured nozzle has been designed. The nozzle is made of aluminum and is composed by two joint parts in order to facilitate machining. **Figure 4** shows a cross section of the nozzle, with the Mach number field computed by means of CFD simulations. The design of additional nozzles for higher Mach numbers up to 9 is planned for the next future.

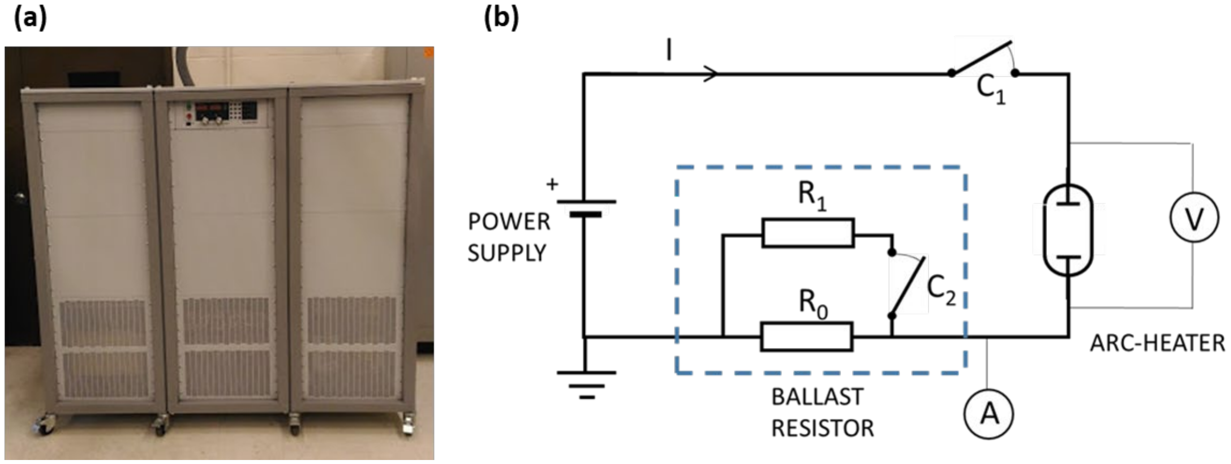

Figure 5. (a) Magna Power M series 250 kW DC power supply; (b) a schematic of the power feeding circuit of ACT-II.

The nozzle is directly connected to the test section of the facility where the combustion experiments take place. The lateral and top sides are provided with elongated quartz windows covering almost the entire length in order to have full access of the internal space for diagnostics, whereas the bottom side hosts several interfaces for electrical, pneumatic and signal feedthroughs. The test section is kept at vacuum pressure (10^{-2} mbar) during the test in order to maintain the flow in over-expanded conditions. Since the rise of the background pressure represents the principal limitation to the duration of the test, the test section is connected to a vacuum chamber with a total volume of about 4 m^3, continuously evacuated by a two-staged Edwards GXS dry pumping system with a total pumping speed of 2000 m^3/h. This allows to reach test-times up to 1 second. An extension is attached to the vacuum tank in order to provide additional space for the installation of the laser sheet-generating optics or other instrumentation. The extension has two lateral circular windows used as access ports for the laser beam.

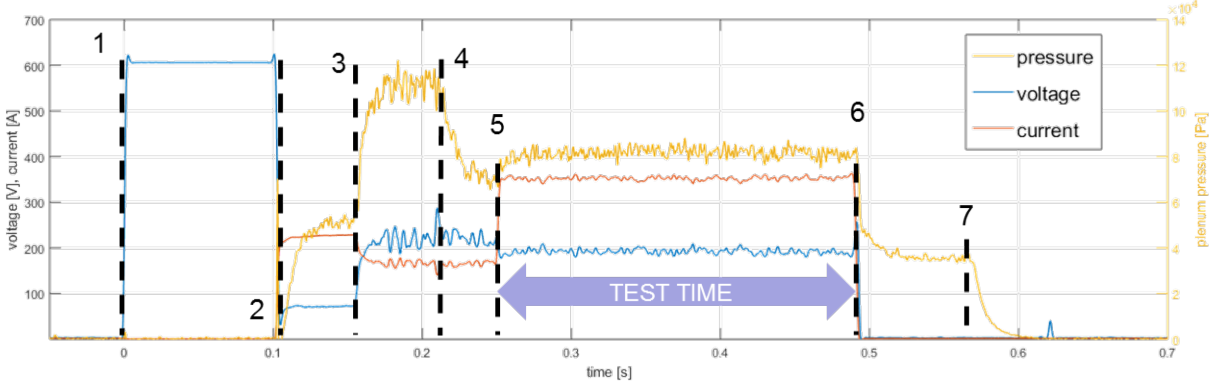

Figure 6. Typical pressure, voltage and current of the electric discharge measured inside the ACT-II arc-heater during a test.

The arc-heater is powered by a 250 kW Magna Power Series M unit (**Figure 5**), a fast-response, fully programmable DC power supply able to provide voltage up to 600 V and current up to 400 A. The power supply terminals are connected to the electrodes of the arc-heater and to the ballast resistor as shown in Figure 10. To trigger the breakdown of the plasma, the high voltage is applied impulsively to the arc-heater using a contactor. The ballast resistor is necessary to stabilize the current in the first instants after the ignition of the arc, preventing overcurrent problems in the power supply. After the discharge is stabilized the resistance can be decreased using a second contactor that connect a second resistor in parallel with the first one. In this way it is possible to maximize the amount of power that can be deployed into the arc. An example of the operations of the arc-heater is shown in **Figure 6**, where voltage, current and pressure of the arc are plotted vs time for a typical test. The sequence is labelled as follows:

1) The first contactor C_1 is closed and a voltage of 600V is applied to the electrodes of the arc-heater while they are still in a vacuum.
2) Argon is introduced into the arc chamber and the electric discharge is initiated by voltage breakdown.
3) Transition to air begins by opening air valves while argon is still flowing.
4) Transition is completing by closing argon valves. From this point on the arc is in nitrogen only.
5) The second contactor C_2 is closed and resistors R_0 and R_1 are connected in parallel reducing the overall resistance and increasing the current accordingly. At this point the useful test time begins. As shown in the figure, the parameters of the arc are remarkably stable during the test time, which can be extended up to nearly 1 second.

6) The power is cut off and the arc extinguished. Cold air is blown through the arc-heater to lower the temperature of the electrodes and insulating parts.
7) Air valves are closed and the test is terminated.

An extensive characterization of the facility stagnation conditions has been performed, in particular for the enthalpy. An accurate knowledge of the stagnation enthalpy is essential to properly analyze the experimental results, but this quantity is not straightforward to measure directly, especially for a pulsed facility. In the present work, the results from two different methods have been compared to reduce the overall uncertainty. The first method is based on the measurement of the temperature at the stagnation point of a probe placed in the supersonic free stream. The probe has a spherical nose and is instrumented with a fast-response (<1 μs) thermocouple, flush-mounted at the stagnation point (**Figure** 7a). A typical temperature signal is shown in **Figure** 7b. The corresponding heat flux can be computed by solving numerically the 1D Fourier equation in spherical coordinates (see **Figure** 7c). Finally, using the Sutton and Graves [Sutton] correlation it is possible to relate the heat flux to the stagnation enthalpy of the gas

$$h_0 = h_w + K_{SG}\,\dot{q}_w\sqrt{R_w / p_{0s}} \tag{1}$$

where $K_{SG} = 3.5\times10^{-4}$ m kg$^{-1/2}$, is the gas enthalpy at the wall, R_w is the radius of curvature of the wall and p_{0s} is the stagnation pressure after the normal shock. To account for uncertainties related to shape and material of the probe, four different probes have been used having different nose radius (4 and 6 mm) and material (stainless steel 410 and constantan).

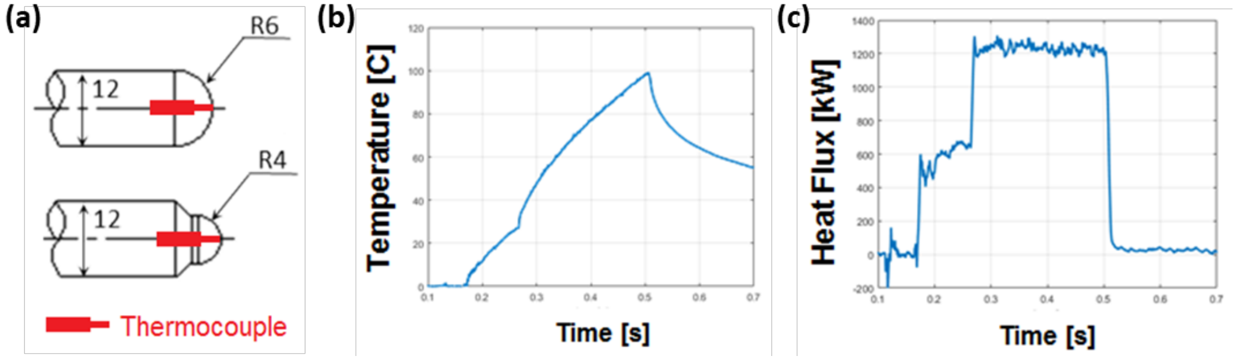

Figure 7. Summary of the stagnation enthalpy measurement procedure using temperature probes. (a) Geometry of the probes. (b) Typical temperature profile at the stagnation point. (c) Heat flux computed from the temperature trace.

The second method is based on the conservation of mass in a control volume enclosing the arc-heater. The mass balance in a control volume enclosing the arc-heater requires that the mass flow rate through the sonic throat of the nozzle $\dot{m}_{noz}$ equals the sum of the inlet mass flow rates of oxygen $\dot{m}_{O_2}$ and nitrogen $\dot{m}_{N_2}$, namely

$$\dot{m}_{noz} = \frac{p_0 A^*}{\sqrt{RT_0}}\sqrt{\gamma}\left(\frac{2}{\gamma+1}\right)^{\frac{\gamma+1}{2(\gamma-1)}} = \dot{m}_{N_2} + \dot{m}_{O_2} \tag{2}$$

where p_0 and T_0 are stagnation pressure and temperature respectively, A^* is the throat area and R and γ are the specific constant and specific heats ratio of the gas. Since A^* is known and p_0, $\dot{m}_{O_2}$ and $\dot{m}_{N_2}$ can be measured, equation (2) can be solved for T_0. Assuming thermodynamic equilibrium, the stagnation enthalpy can be computed as $h_0 = h_0(T_0, p_0)$. Note that being both R

and γ functions of the equilibrium composition of the gas, and therefore of p_0 and T_0, equation (2) must be solved iteratively.

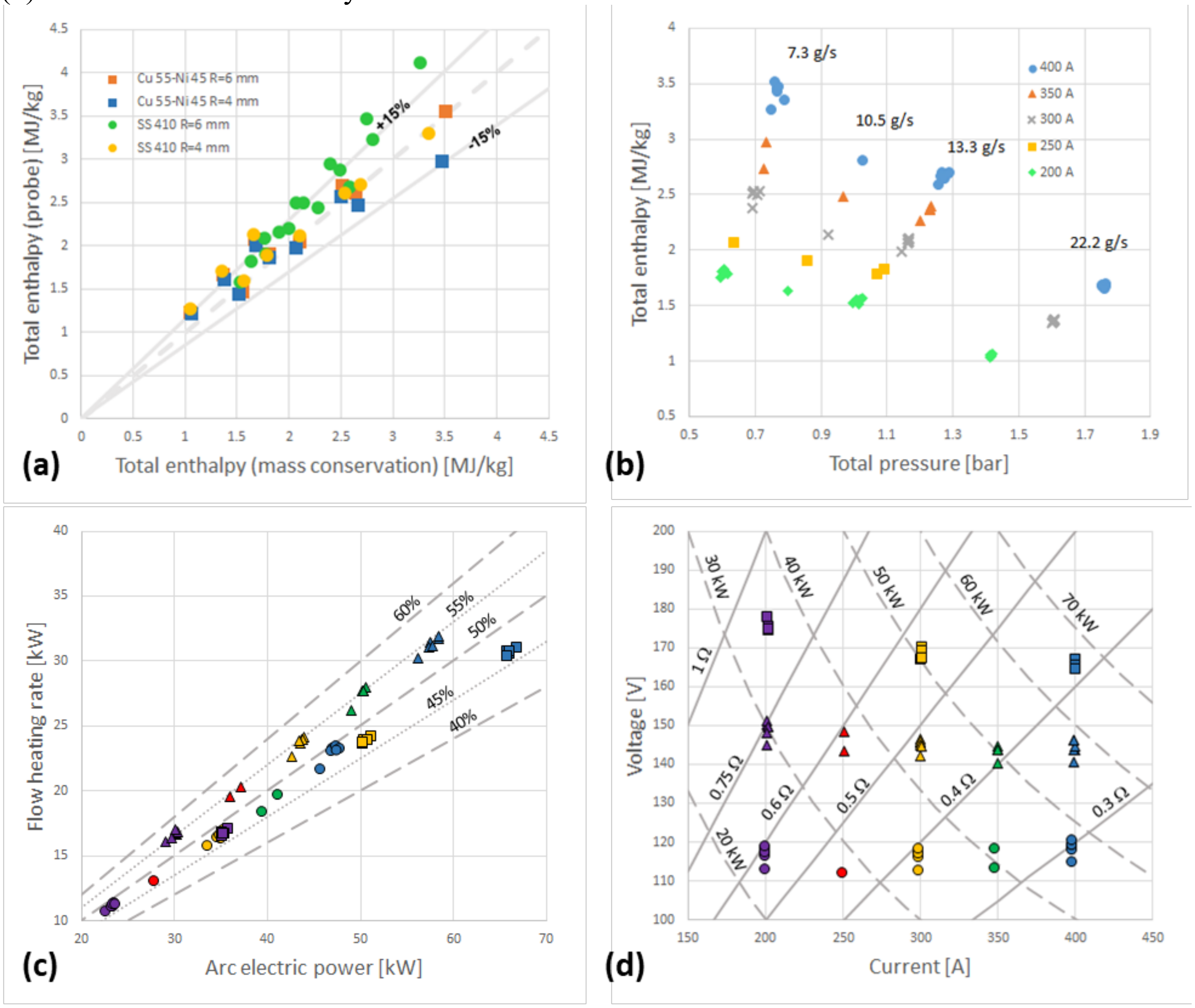

Figure 8. (a) Total enthalpy of the gas measured by the temperature probes vs the corresponding value estimated by mass conservation considerations (Eq. 2); (b) Total enthalpy vs total pressure chart, as function of current and mass flow rate of the arc-heater; (c) Heating rate of the flow plotted vs the electric power of the arc as function of current and mass flow rate in the arc-heater. (Color legend. Blue: 400 A, green: 350 A, yellow: 300 A, red: 250 A, purple: 200 A. Symbol legend. □: 22.2 g/s, Δ: 13.3 g/s, ○: 7.3 g/s); (d) Arc voltage plotted vs current as function of current and mass flow rate in the arc-heater. (Color legend. Blue: 400 A, green: 350 A, yellow: 300 A, red: 250 A, purple: 200 A. Symbol legend. □: 22.2 g/s, Δ: 13.3 g/s, ○: 7.3 g/s).

The results of the measurements are presented in **Figure 8**. In **Figure 8**a, the total enthalpy computed from mass conservation is used as reference to compare the results obtained with the temperature probes. All the experiments were carried out using a mixture composition (by volume): 80% nitrogen and 20% oxygen. The temperature probe was placed on the nozzle axis with the tip aligned with the exit plane. Several values of current (between 200 A and 400 A) and mass flow rate (between 7.3 g/s and 22.2 g/s) were tested for each of the four probes. Most of the data from the temperature probes fall within a ±15% range around the value computed from mass conservation, showing a good agreement between the two methods.

Figure 8b shows the stagnation conditions of the flow as function of the control parameters of the facility, namely current and mass flow rate. The stagnation pressure can be varied in a range of 0.6 to 1.8 bar, whereas the stagnation enthalpy can be increased from room conditions to 3.5 MJ/kg. In **Figure 8**c, the gas heating rate $\dot{m}\,\Delta h_0$ is plotted versus the electric power of the arc VI. In this case, the same color corresponds to the same current, whereas the same marker shape is used to indicate same mass flow rate. The slope of the lines on this chart represents the thermal efficiency of the heating process according to the energy balance $\dot{m}\,\Delta h_0 = \eta_{th} V I$. For the present configuration of the arc heater, the efficiency ranges from 46 to 55%. As shown in the figure, the efficiency does not depend appreciably on the current. This result, in agreement with the theory of Stine and Watson [Stein], is expected to hold as far as the temperature is low enough for the radiation losses to be negligible. **Figure 8**d shows the voltage drop versus the arc current for each one of the tests performed. The characteristic of the arc exhibits a neutral or slightly negative slope as expected in this range of current. The value of the voltage drop across the electrodes is strongly affected by the mass flow rate of the gas, ranging from 100–110 V at 7.3 g/s to 165–175 V at 22.2 g/s. Also, the slope of the characteristic changes, becoming more negative when the mass flow rate is increased. Iso-lines for total electric power (dashed) and static resistance (solid) of the arc are shown on the same chart for reference.

5. NANO-SECOND LASER INDUCED BREAKDOWN SPECTROSCOPY (LIBS)

Nanosecond-gated laser induced breakdown spectroscopy (nano-LIBS) measurement concept allows for fuel concentration and gas density information to be obtained in highly reactive and high-speed environments such as those found within high-speed airbreathing engines. The technique is based on laser induced plasma breakdown spectroscopy, in which a laser is focused to produce a small volume of plasma at the desired measurement location. The emissions of this plasma are captured and the properties of the test medium prior to formation of the plasma can be determined. Emission collection must be done at a time frame much shorter than typical LIBS measurements in order for the measurement to be made before the plasma can affect the flow field, or the fast-evolving reacting environment can influence the plasma emissions. In previous works, the collection has been done on the order of milliseconds which is too long for use in high speed flows [Miziolek, Musazzi, Reinhard]. Nano-LIBS has been developed in conjunction with a new direct spectrum matching (DSM) technique for the quantification of fuel concentration and gas density information. In addition, multiple experimental layouts have been evaluated that allow for experimentation using only one optical access point.

While the majority of the time LIBS is used to determine the atomic composition of solids through a process of laser ablation and subsequent plasma formation in the dissociated plume, it has also become an important measurement technique for quantitatively determining gas properties [Blevins, Do, Do, Ferioli, Sturm]. A laser beam is focused such that there is sufficient energy at the focal point to ionize, dissociate, and excite molecules in a small volume at the focal point. The plasma forms in a small sphere and then the plasma develops through cascade ionization and propagates up the incoming laser beam forming a truncated cone approximately 1 mm^3 in volume [Brewczyk, Cremers,Yalcin]. The excited species within the laser induced plasma then emit photon emissions that contain information regarding the atomic composition and gas density of the target gas prior to the formation of the plasma. Atomic compositions of the plasma determine the spectral profile of the emission and individual emission line strength, while overall emission strength and line broadening effects are determined by the gas density.

The DSM process quantifies the properties of the gas through the matching of the spectra with a spectrum from an intensive database that covers the range of gas density and fuel concentrations found in the desired testing environment. The database is constructed by producing plasma emissions in well-known gas conditions. Two comparisons are needed in order to completely match a spectrum with the database. The first comparison matches the gas density and is done by comparing the full width half max (FWHM) of a certain emission line with the spectrum normalized by the selected line, in this case the oxygen line at 777 nm was chosen as it was sufficiently strong and relatively isolated. Construction of the database was performed in a variable pressure combustion chamber (VPCC) that allowed for pressures between 700-50 Torr. Since the fuel to be used in the model combustor was known to be ethylene mixtures of ethylene and air were used to perform the calibration experiments with fuel concentrations between X_{C2H4}= 0% - 30%.

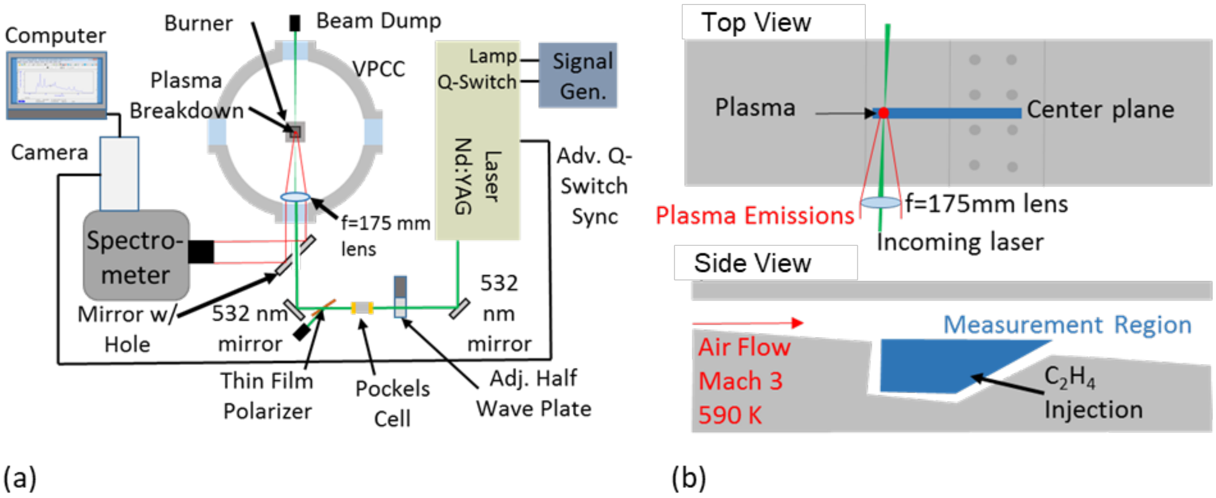

Figure 9. (a) Setup for construction of direct spectrum matching database. Setup is centered on the variable pressure combustion chamber. (b) RC-19 tunnel setup. Plasma breakdown is moved throughout the cavity to completely map the fuel concentration and gas density.

Figure 9a shows the experimental setup used for the construction of the spectra database used in the DSM process. A variable pressure combustion chamber (VPCC) is used to create different gas density by varying the ambient pressure of the gas in which the plasma probe is formed. The database consists of spectra taken between 50 and 500 torr at 293K which covers the range of gas densities found in the reacting combustor environment. The plasma probe is produced with a Nd:YAG laser (Spectra Physics GRC-170) frequency doubled to 532 nm and operating at 10 Hz. Laser power is controlled through the use of an adjustable half wave plate, pockels cell, and thin film polarizer setup. By rotating the half wave plate and controlling the voltage differential across the pockels cell the amount of energy directed into the focusing optics can be adjusted without changing the spatial or temporal profile of the laser beam. Additionally, the pockels cells allows for the plasma probe to only occur during the optical capture process, and not before. Laser power was set to 100 mJ per pulse for the course of the experiment. The laser is focused with a 175 mm bi-convex lens 2 mm above a modified premixed Hencken burner.

The burner exit is 25.4 mm x 25.4 mm surrounded by a 10mm inert gas shroud. Flow controllers are used to create mixtures of air and ethylene (C_2H_4) with fuel mole fractions between 0-30%. Plasma emissions are collected in a backscatter direction with a holographic spectrometer (Kaiser Holospec f/1.8) and captured with an intensified CCD camera (Andor iStar DH320T-18U-

73). A wavelength range of 550 nm – 800 nm is captured and used for analysis. Laser scattering at 532 nm is blocked with a long pass filter (Semrock BLP01-532R-50) prior to the focusing optics of the spectrometer. The camera operates with a 10 ns gate and is delayed 85 ns (5 ns jitter) from the start of plasma emissions, for a total measurement time < 100 ns.

Measurements were taken in Research Cell 19 (RC-19) located at Wright-Patterson Air Force Base in a collaboration with Air Force Research Laboratory. RC-19 contains a continuous supersonic wind tunnel. During experiments the tunnel was setup to operate at Mach 2 with an inlet temperature of 590 K. The wind tunnel houses a direct-connect model scramjet containing a flame-holding cavity. The experimental setup used in RC-19 is shown in **Figure 9**b. Fuel (C_2H_4) was injected from the back ramp of the cavity in the upstream direction. Measurements were taken throughout the cavity using the same laser and camera setup as with the VPCC through the use of a 3-axis table that can move relative to the tunnel. Measurements were taken on the center plane of the tunnel as well as 1 inch off center. The laser spark served as an ignition source. The tunnel has a width of 152.4 mm and a divergent bottom wall with angle 2.5 degrees from parallel. The refresh time scale of the cavity is on the order of 1 ms, thus for this experiment at 10 Hz measurements are not affected by previous plasmas/measurements except in the case that the flow field is ignited. It was found that n-LIBS was a successful method for the simultaneous gas density and fuel concentration measurements in the high-speed reacting environment found in the cavity. An example of the fuel concentration measurements can be found in **Figure 10**. The fuel concentration throughout the cavity is shown as well as the points at which measurements were performed.

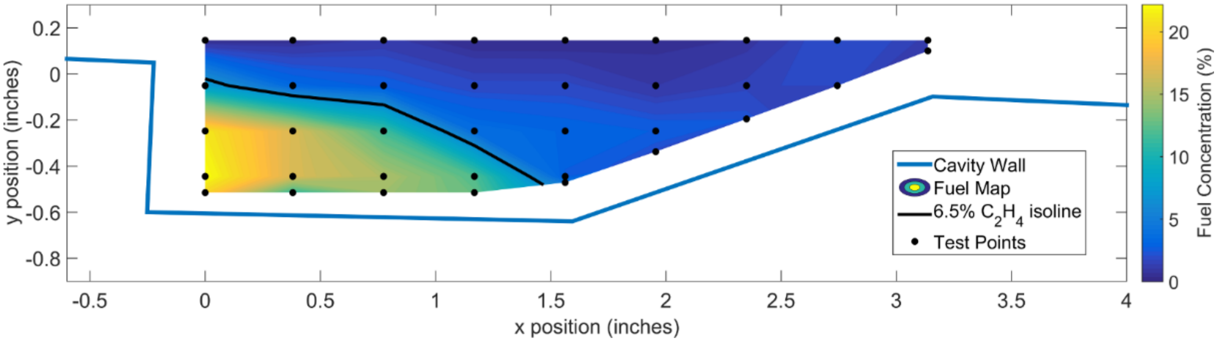

Figure 10. Fuel concentration map within the flame-holding cavity on the centerline. Highlighted is the 6.5% isoline and the points at which measurements were taken.

During the course of the experiment it was found that the emission spectrum of a gas depends on gas density and atomic number ratios only, not the mother species. This is visualized in **Figure 11** which shows 3 spectra taken under different conditions. The first spectrum was taken in a mixture of C_2H_4 and air with $X_{C_2H_4} = 6\%$ at atmospheric pressure (760 Torr) and downstream of the flame front in the hot product gases. The second spectrum was taken with the same gas mixture at a much lower pressure, 100 Torr, but the probe was positioned upstream of the flame front with a temperature of 293K. The two spectra are identical indicating that the *T*/*P* ratio is the same for both conditions. The third spectrum was acquired from a mixture of CH_4, N_2, O_2, and CO_2 at 100 Torr and 293 K, which was designed to have the same atom ratios as the first two cases. This spectrum is once again identical to the previous two cases. With this concept gas mixtures can be created in which a single atom ratio is varied in order to see the effect on the spectra.

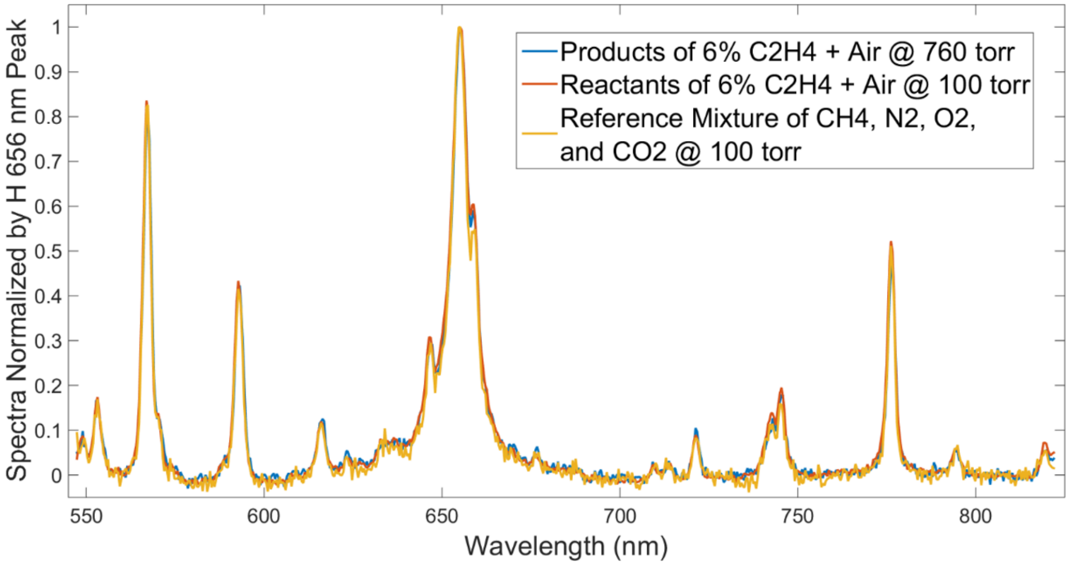

Figure 11. Spectra obtained from three gas conditions showing the dependence of the spectra on gas density and atomic ratio and independence of mother species.

In this manner the spectra can be "tuned" to match an unknown sample. This could be a useful technique for future work where individual emission lines need to be adjusted independently to form a spectrum database.

Measurements were taken in a flameholding cavity located in a scramjet combustor, with a Mach 3 core flow and stagnation temperature of 612 K. A flow disruptor was introduced to determine how fuel and air mixing was affected by the addition of an impinging oblique shock wave on the shear layer above the flame holding cavity. The same optical setup is used as with the DSM database construction setup. The optics and laser are mounted to a 3-axis table such that the probe location can be moved throughout the cavity. A total of 45 locations are probed in a grid pattern based on previous measurements in the tunnel along the center plane. Ethylene fuel is injected from the sloped closeout ramp at the downstream side of the cavity in a direction opposite the core flow. The fuel flow rate was kept at 56 standard liters per minute for the course of the experiment. To accurately characterize an environment with highly variable temperature and pressure, the direct spectrum matching (DSM) method was used. This method compared the effects of gas density and fuel concentration to match an unknown spectrum with one from a database that covers the range of gas density and fuel concentration found in the test environment. As shown in a previous work, the DSM process allows for quantitative measurements of fuel concentration and gas density (pressure/temperature ratio).

Figure 12 shows the two positions of the shock inducing wedge used in the course of the experiment. Three different test conditions were used during the course of the experiment. The first was with no wedge present. The second was wedge position 1, in which the oblique shock from the front of the wedge is positioned at the front step of the cavity. The third is wedge position 2, in which the oblique shock is positioned at the center of the cavity. The shock from the wedge is used to mimic the shock train that develops from the inlet and isolator sections of a real scramjet. As the tunnel used to conduct these experiments is a direct connect type tunnel, there is no inlet and thus there is no shock train. By positioning a wedge on the top of the tunnel slightly before the cavity, a shock can be produced to mimic the shock from the inlet, and the way that the shock position affects the fuel-air mixing inside the cavity may be investigated.

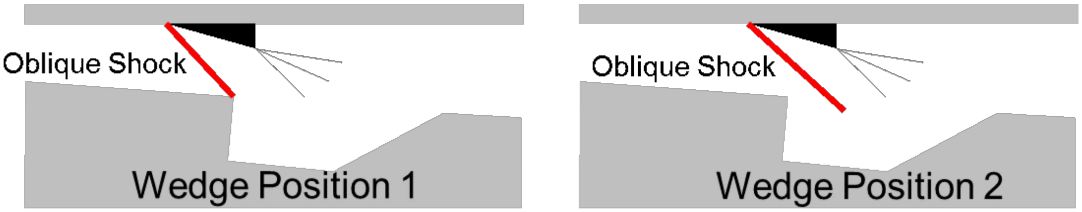

Figure 12. Two wedge positions were used in the experiment. Wedge position one results in an oblique shock impinging on the front step of the cavity. Wedge position two results in a shock impinging on the center of the cavity.

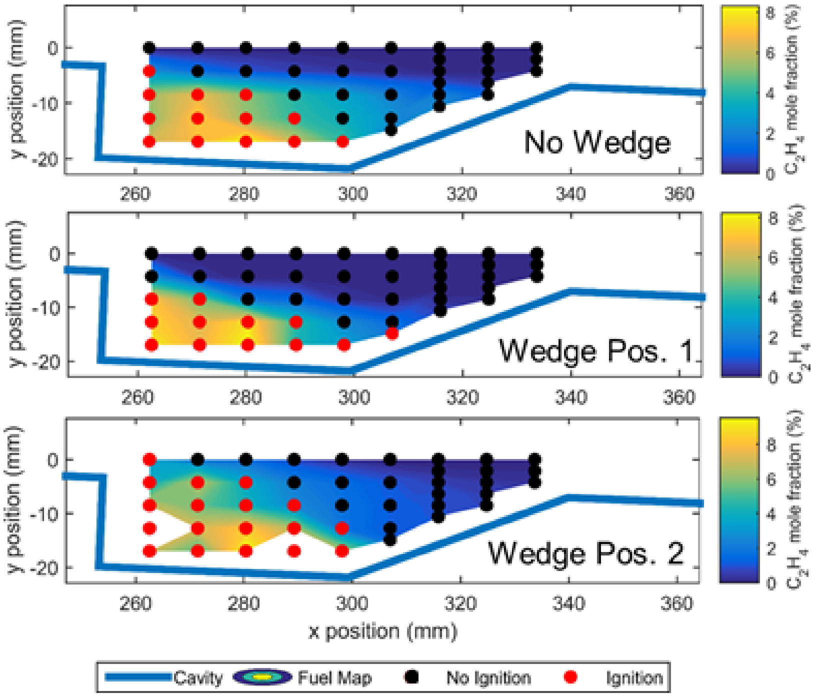

Figure 13. Fuel mole fraction for the three shock inducing wedge positions. The shock results in a change in the shape of the recirculation zone.

Figure 13 shows the quantified results from the RC-19 measurements taken for the three shock conditions, no wedge, wedge position 1, and wedge position 2. All measurements were taken in the non-ignited case. At each point a series of measurements were taken and the results shown are the average of those measurements. At points were the plasma probe did not result in ignition a total of 300 measurements were taken. At points were the plasma probe resulted in ignition a variable number of measurements were taken, depending on the number of pulses before ignition occurred. AS can be seen in the figure, all three cases resulted in a similar maximum local fuel mole fraction of about 8%, slightly above stoichiometric (6.5% C_2H_4), in the lower front part of the cavity. In the no wedge case, the shear layer can be seen extending from the front step roughly parallel to the bottom wall towards the closeout ramp. The shear layer can be visualized as the region with the sharp drop to a zero fuel mole fraction. In the wedge position 1 case the shear layer is deflected downward due to the impinging shock and a smaller recirculation zone is realized. In the wedge position 2 case the recirculation zone is increased in size and extends in a region above the front step. The points at which ignition was possible are also extended and a point above the front step was found to result in sustained combustion.

Fuel surrogates was introduced to better characterize fuel concentrations and statistics in the ignitable region of the cavity for the non-combusting case. During previous measurements at locations where the cavity was ignited by the laser breakdown were limited typically to under 5 measurements per location. In order to gain understanding of the fluctuations of fuel concentrations at these points, CO_2 is used instead of the typical C_2H_4 and is injected through the same upstream facing nozzles along the closeout ramp of the cavity, as well as the cross flow jets upstream of the front step, at the same injection pressures at fuel. Using the fuel surrogate as many tests as desired can be taken at each measurement location without having to reset fuel and tunnel temperatures each time. However, in order to use the fuel surrogate, an additional calibration table was required to be constructed.

The DSM matrix for both C_2H_4 and CO_2 was improved with an increased density between fuel mole fractions. In previous years the DSM matrices were constructed with a step size of $X =$ 2.5% between fuel mole fractions. During year IV the step size for the DSM matrix was reduced to $X = 0.25\%$. It was found in previous years that the uncertainty at low fuel mole fractions was not sufficient. By increasing the DSM matrix density, the uncertainty for both gas density and for fuel mole fraction can be reduced.

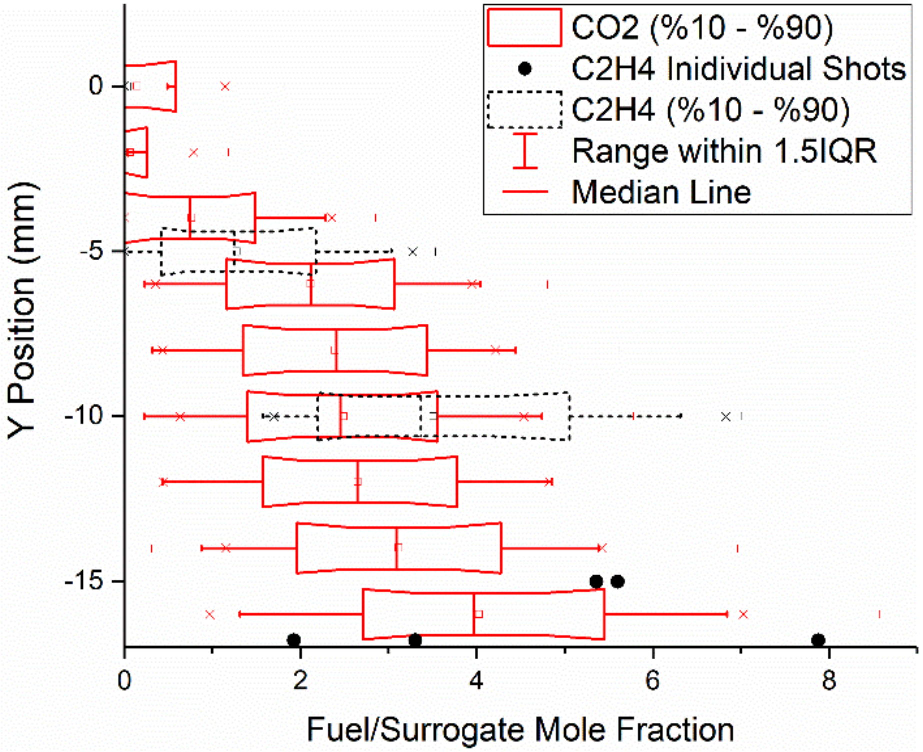

Figure 14. Comparison of results for n-LIBS cavity flameholder of dual mode scramjet combustor with both C2H4 and CO2 injection.

Figure 14 shows a comparison between measurements taken with C_2H_4 and CO_2 fueling in the cavity flameholder. When the cavity is fueled with ethylene the n-LIBS measurements will cause sustained combustion in the cavity at certain locations. As it would be time prohibitive to conduct sufficient tests in order to build a statistically significant data set the use of a fuel surrogate allows for the collection of a large number of individual measurements. Additionally, the measurements at points that can result in ignition may be biased towards local fuel mole fractions which are too low to result in sustained combustion.

6. CH PLANAR LASER INDUCED FLUORESCENCE (CH-PLIF)

Significant advance in imaging of flame dynamics was made by the PI and Dr. Carter (AFRL) that held promise to revolutionize the diagnostics of turbulent flames. It is a breakthrough that enables us to image the dynamic motion of the flame front with unprecedented clarity and at high temporal resolution. The novel strategy evolves around a new transition of the CH radical (C−X transition), which enables PLIF images to be obtained with up to two orders of increased efficiency. This translates to detailed images which can be extended into the kHz regime [Carter], enabling a revolutionary advance in implementation of high speed imaging for turbulent combustion diagnostics.

Imaging of CH has always posed problems for PLIF even with the previous high power systems at low frame rates. Here, we will employ the novel technique of using the $C^2\Sigma^+$−$X^2\Pi$ (v'=0,v''=0) [Chou, Jeffries, Hirano] band near 314 nm where excitation and emission efficiencies are significantly larger than the traditional $A^2\Delta$–$X^2\Pi$ (0,0) and $B^2\Sigma^-$−$X^2\Pi$ (0,0) transitions [Carter]. While the C state is strongly predissociated [Luque, Ubachs], the fluorescence yield is not significantly affected at atmospheric pressures and above, as electronic quenching should be the dominant decay mechanism ($Q_{e,C} > 2.5 \times 108\ s^{-1} \geq Q_{predis}$), as noted by Jeffries et al. [Jeffries]. Moreover, the C−X(0,0) emission coefficient is large, ~9 × 106 s^{-1}, as are the absorption coefficients; for example, for most Q-branch transitions, $B_{12} > 2.5 \times 1010\ m^2\ J^{-1}s^{-1}$ [Luque]. As a result, even with a 314-nm pulse energy of 0.1 mJ and a laser sheet size of 75 mm × 0.3 mm, the excitation rate with an 8-ns laser pulse is ~$10^9\ s^{-1}$, which can be easily achieved with the high speed dye laser based systems of the PIs. Of course, there are OH $A^2\Sigma^+$−$X^2\Pi$ (0,0) and (1,1) transitions nearby, but this can be utilized for potentially simultaneously imaging of CH and OH with one laser and one camera as shown in **Figure 15**.

The low laser energy requirements of the new strategy enable this method to be used for the continuous high speed dye laser systems we have today. The 314 nm required for the transition can be easily obtained with a conventional setup using the DCM laser dye. Figure 3 shows an example of the CH C−X(0,0) PLIF at high framerates [Carter]. Furthermore, the highly efficient transition offers a means to volumetrically illuminate CH contours in space, opening the way for acquiring unprecedented 3D information.

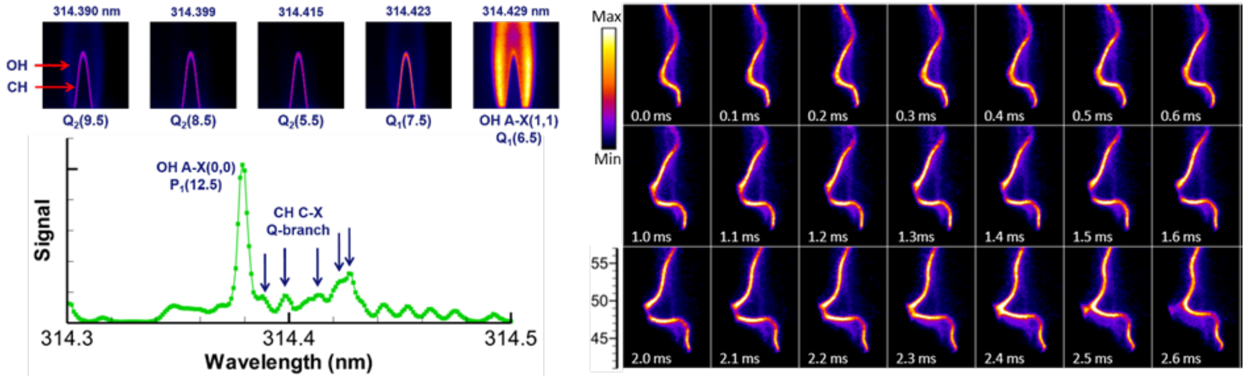

Figure 15. CH C−X(0,0) excitation scans (left) and high speed PLIF imaging at 10 kHz (right). Simultaneous OH and CH PLIF imaging can be obtained by wavelength modulation. Note the SNR (exceeding 25) at 10 kHz framerates (right).

In addition to the high-speed imaging of CH, the efficiency of the C−X transition allows volumetric excitation of flame fronts, which can be imaged using a multi-camera setup. A demonstration was carried out at WPAFB in collaboration with Professor Lin Ma (Virginia Tech). The results show that the new method has incredible potential as a means of imaging flame front propagation in a turbulent environment. These measurements were made using a series of 5 cameras (combination of SA-5 and SA-Z with LaVision high-speed intensifiers) surrounding the turbulent combustor. The reconstruct 3D surfaces of CH contours in the flame is shown in **Figure 16**.

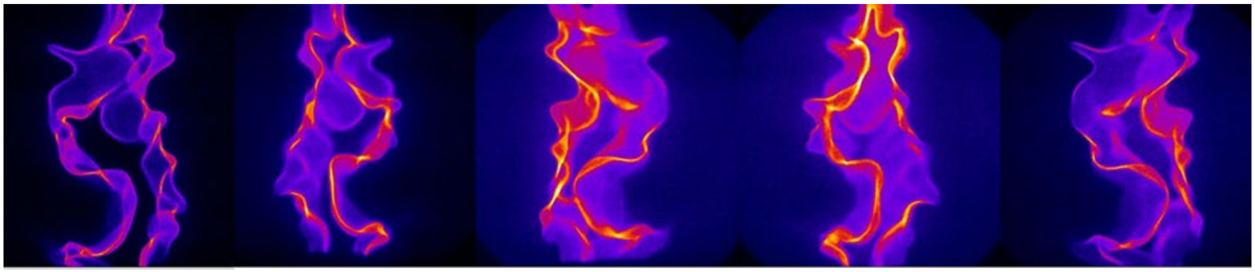

3D Volumetric CH Contours of Turbulent Flames

Figure 16. Demonstration of 3D multi-axis imaging of the CH layer in a high shear turbulent flame in collaboration with Dr. Campbell Carter (AFRL) and Dr. Lin Ma (Virginia Tech). Images taken in July of 2015 at AFRL with lasers from University of Illinois.

The novel strategy of using the CH radical (C−X transition) have been able to apply this technique to a practical laboratory turbulent jet flame (Hi-Pilot Burner from University of Michigan). The nearly two orders of increased efficiency of the C−X transition enables a revolutionary advance in implementation of high speed imaging extended into the kHz regime for turbulent combustion diagnostics. The low laser energy requirements of the new strategy enable this method to be used for the continuous high speed dye laser systems. The 314 nm required for the transition can be easily obtained with a conventional setup using the DCM laser dye. **Figure 17** shows an extension of this to the Michigan Hi-Pilot burner in collaboration with Professor Jim Driscoll's group and AFRL (Dr. Campbell Carter). In the right inset of **Figure 17**, we carefully tuned the excitation so as to capture both CH and OH simultaneously with one laser and one camera system.

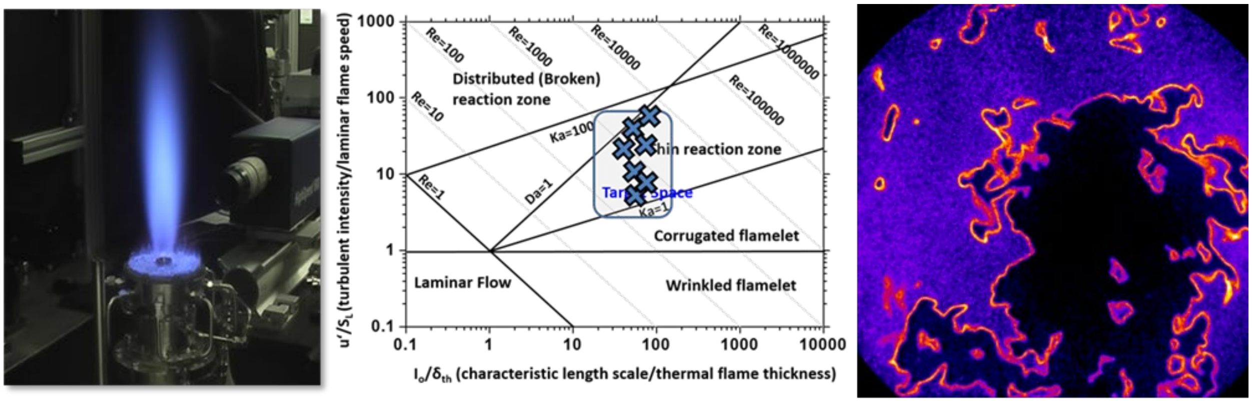

Figure 17. CH C–X(0,0) PLIF in the Michigan Hi-Pilot. The combustor is shown in the left, the turbulent flame regimes are shown in the center and an example of a simultaneous CH and OH excitation with one laser and detector are shown in the right.

The main drawback to this method is in the resonant transition characteristics. Several strategies are being developed to resolve this issue, which can minimize the laser scattering from the surrounding combustor surfaces. One strategy that will be investigated is to utilize a satellite

R transition (R_{13} seems to be a promising candidate) and then use a sharp filter to cut off the laser scattering. This may require the design and construction of an extremely sharp edge filter (cutoff from 10 to 85% within 2 nm range), as well as careful modulation of the excitation wavelength. Another strategy can be to use the relative differences in the polarization of the CH-PLIF signal and the scattered sources.

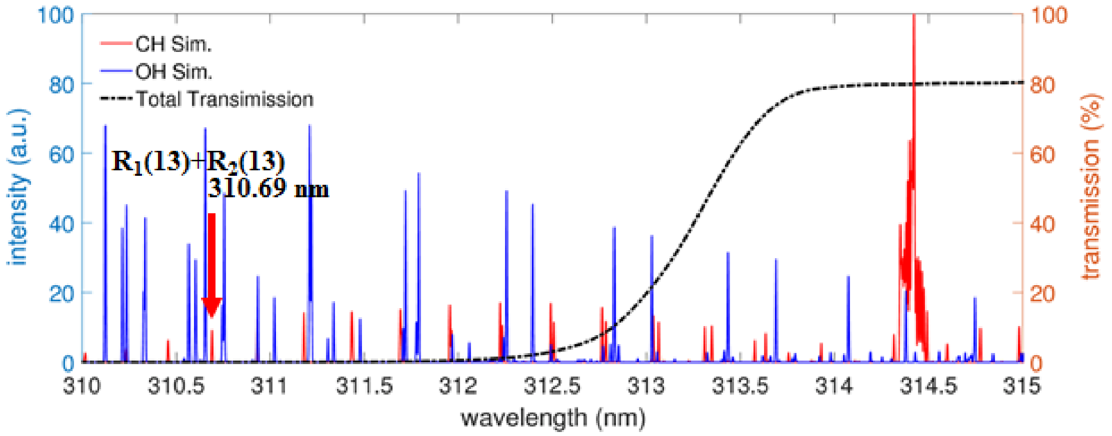

Figure 18. Simulated excitation spectra for OH and CH with custom filter stack transmission properties.

Most of the previous work detailing this transition focused on the excitation band near 314 nm. One disadvantage in using the aforementioned transition, is that the excitation and emission wavelengths are very similar, and as such detection limits are very prone to scattering and reflecting surfaces. Therefore, it works very well in open flame burners, where scattering is minimal and can be avoided. In order to combat this problem, we decided to target a slightly different rotational excitation transition in the same vibrational band, near 310 nm. The fluorescence collection wavelength remained at around 314 nm. This allows for the separation of the excitation and emission wavelengths, essentially eliminating the previous problems with scattering, and allowing the application of this novel strategy to more complex burners or combining with other diagnostic techniques previously not possible, like PIV. However, in order to ensure that the excitation and emission wavelengths were fully separated, at the collection optics, a custom sharp filter stack was developed, as shown in **Figure 18**.

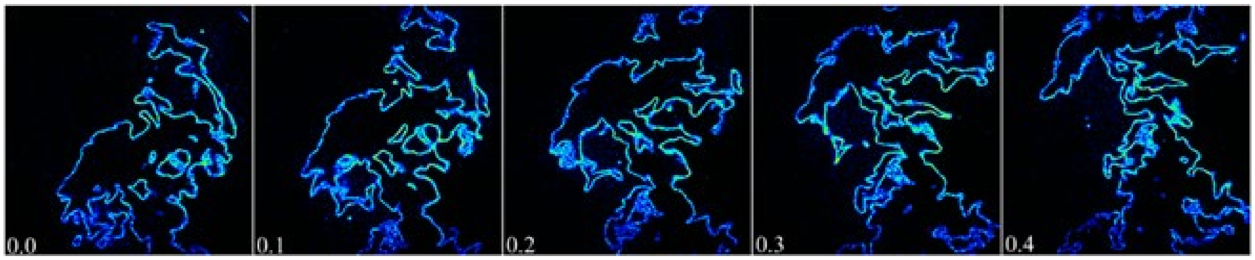

Figure 19. CH C–X(0,0) PLIF in the Michigan Hi-Pilot with 310.69 nm excitation wavelength. Time evolution is shown in the bottom left of each segment in ms.

The 310 nm required for the transition is obtained similarly as before, using a conventional setup, Nd:YAG coupled with a Dye laser, with DCM as the laser dye. **Figure 19**, illustrates a time sequence taken at 10 kHz of the transition on the Michigan Hi-Pilot burner in collaboration with AFRL (Dr. Campbell Carter and Dr. Stephen Hammack). Similar to the 314 nm excitation scheme, several OH lines are present in the vicinity, which have a twofold role, allowing for easier tuning of the laser system to the target transition, and performing simultaneous CH and OH, with a single laser and camera system.

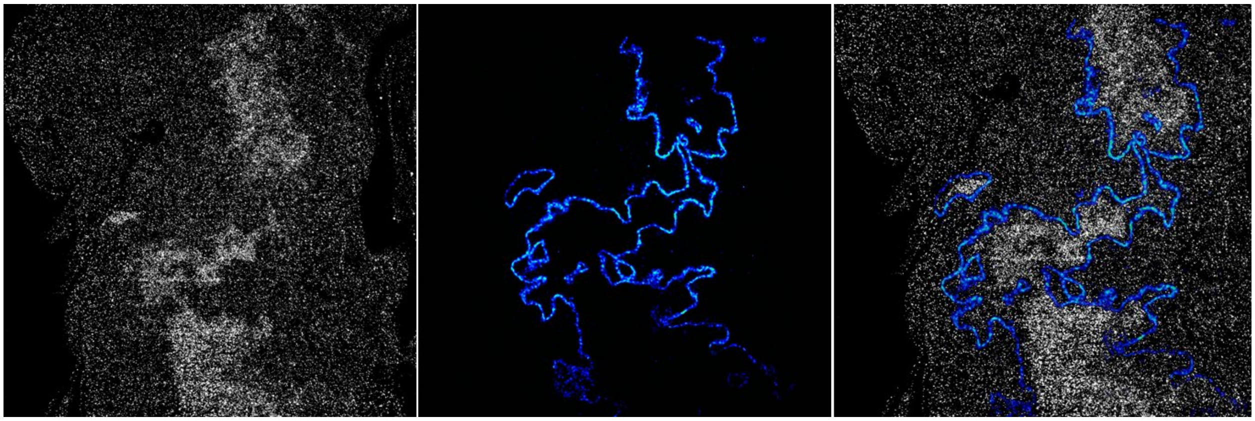

Figure 20. Demonstration of minimal effect of PIV particles on the CH PLIF imaging.

The primary advantage of the satellite excitation transition near 310 nm, is as mentioned, the fact that it allows for separation of the excitation and emission wavelengths. One application of this new transition is to combine it with PIV. For example, the image sequence shown in **Figure 20**, was actually captured simultaneously with PIV. The flow was seeded with TiO_2 particles, which are highly reflective, yet no interference from them can be observed in the PLIF images, as shown in Figure 18. As expected, the particle density changes across the flame sheet, which is nicely tracked by the CH PLIF. Example 2D velocity fields are shown in **Figure 21**, for the average flow field, instantaneous flow field and simultaneous CH PLIF.

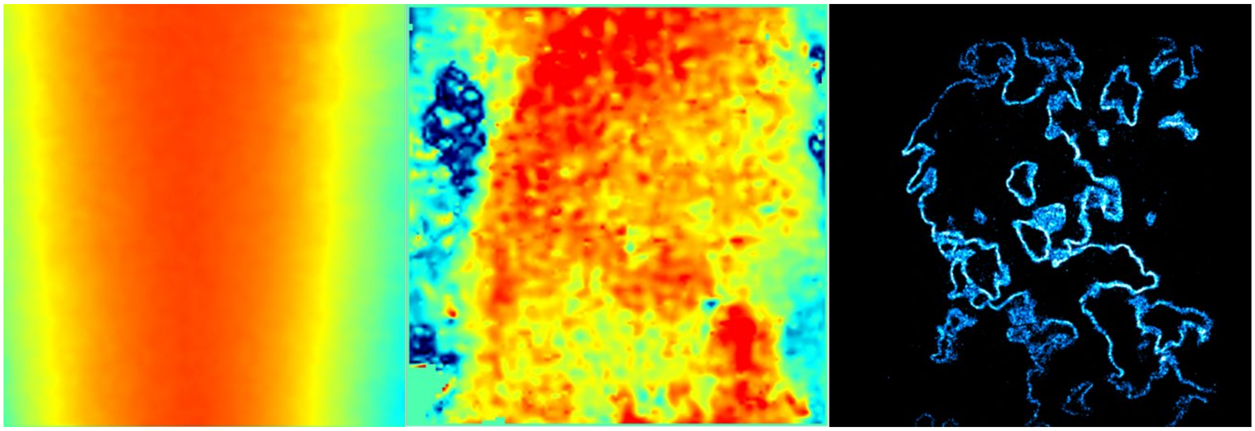

Figure 21. Velocity fields for combusting flow, Average (Left), Instantaneous (Middle) with accompanying instantaneous CH PLIF (Right).

The effectiveness of this transition was demonstrated in a multitude of different burners, ranging from mesoscale to sector rig combustors. Using this method combustion phenomena near the reaction zone can be probed and analyzed at high repetition rates. One problem with the simultaneous PIV and CH in highly turbulent flows is the out of plane motion of the particles, which results in erroneous velocity vectors. One strategy to combat this method is to expand the PIV into a tomographic PIV setup, which will allow for instantaneous measurement of all three velocity components in a complete 3D measurement volume.

7. ACT-II RESEARCH

The circular combustor geometries are used in the experimental studies in ACT-II. The axisymmetric combustors not only limit corner flow effects but also decrease the structural weight required to withstand a specified pressure/thermal load, and the reduced wetted surface area needed to enclose a specific cross-sectional area. The round flowpath design has experienced a revival since the hypersonic community abandoned circular shapes and turned to the rectangular shapes in the late 1960s [Bulman]. Current scramjet inlet design employing the inward-turning streamline-tracing method enables the application of circular isolators/combustors in practical scramjet engine designs. The intrinsic geometry required for the airframe-integrated scramjet modules needs to be rectangular for inlet compression and easy integration [Billig]. The scramjet with rectangular to circular/elliptical shape transition can achieve equivalent performance levels of the 2D rectangular shape with significant weight reduction and the overall mechanical complexity of the system [Smart].

1). DIRECT-CONNECT CIRCULAR CONSTANT-AREA SUPERSONIC FLOW

Inlet unstart is a major issue affecting hypersonic air-breathing propulsion systems. An unstarted engine is characterized by a normal shock standing still in front of the inlet, accompanied by large flow spillage that reduces the air supply to the engine. In addition, the normal shock generates large wave drag with dramatic consequences for the stability of the vehicle. Both external and internal factors can cause inlet unstart. External factors are related to the flight conditions of the vehicle and may include a reduction of the free stream Mach number, excessive flow distortion (such as angularity, non-uniformity, etc.) and pressure losses induced by shock waves or boundary layer separation. Internal factors are related to a backpressure rise inside the engine in consequence of flow choking, occurring when sonic conditions ($M = 1$) are reached at a certain location in the flow field. Choking is more likely to occur when the scramjet is operating in a low flight Mach number range, typically from 3 to 6 (take-over regime) as a consequence of a variety of factors like combustion heat release (thermal choking), area blockage, mass injection, irreversibility, etc. Once the flow is choked, a re-adjustment of the upstream conditions from supersonic to subsonic is necessary in order to recover steady operations [Matsuo].

Figure 22 shows the experimental setup and optical path for the direct-connect combustion configuration. The metallic combustor can be interchangeable with the quartz combustor for flow and flame visualization. The experimental setup consists of a direct-connect circular combustor (I.D. 28 mm) and 400 mm long. The hot air flow is generated by a contoured plug nozzle (Mach 3 nominal). The fuel (ethylene) is injected through four transverse supersonic jets located (Mach 3.3) on the nozzle plug. The combustor can either be a plain quartz tube for flow and flames visualization or a metal tube instrumented with up to 18 pressure transducers and 11 coaxial thermocouples. Stagnation point heat flux and pitot pressure of the exhaust flow were characterized by probes, coaxially mounted at the combustor outlet. The pitot probe intake is at the same axial position of the last pressure transducer (PS18) so that the Mach number at this location can be computed by the Rayleigh-Pitot formula. To evaluate the effects of combustion, each test condition was repeated twice, one injecting fuel and one injecting air. Optical diagnostic tools included planar laser induced fluorescence (PLIF) and chemiluminescence of the OH radical. For high-enthalpy flow testing, the stagnation pressure and temperature for these experiments were 113 kPa and 2.5 MJ/kg respectively. The overall equivalence ratio ϕ varied from 0.58 to 1.0 with choking occurring above ϕ=0.58. For cold flow testing, the freestream has a stagnation temperature of 300 K, total pressure of 3.5 bar.

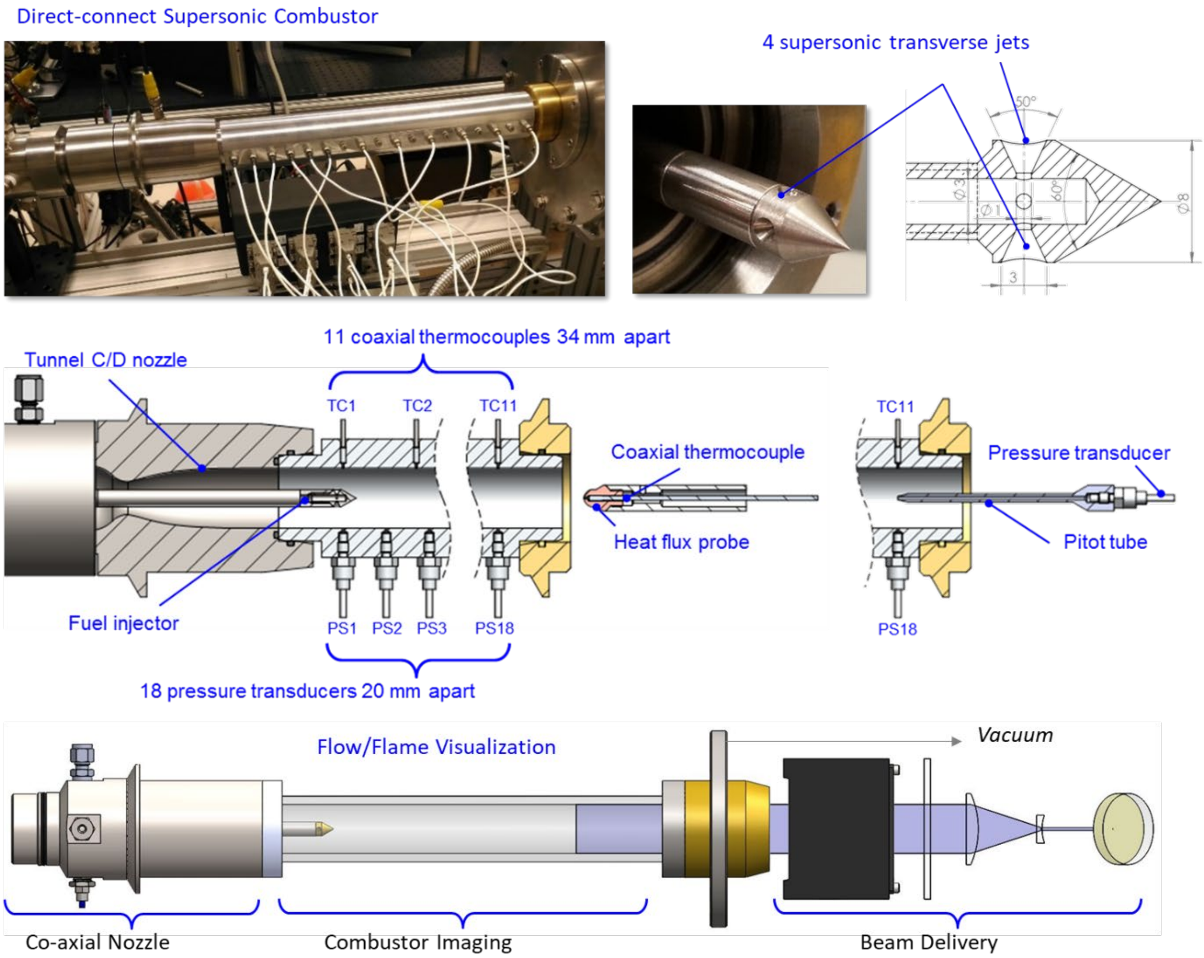

Figure 22. Direct-connect circular constant-area combustor.

Cold flow visualization of the combustor in direct-connect configurations has been performed by condensed CO_2 PLRS (Planar Laser Rayleigh Scattering) technique. **Figure 23** shows the coaxial supersonic jet exiting from the fuel nozzle and interacting with the external flow. The image is realized injecting CO_2 through the fuel nozzle and using pure nitrogen in the mainstream to create enough contrast. The CO_2 feeding pressure is kept constant, but the pressure of the mainstream is changed to create two situations of under-expanded (**Figure 23**a) and over-expanded flow (**Figure 23**b). In under-expanded conditions the jet expands further into the mainstream. The core region of unperturbed flow is limited by the Mach line departing from the edge of the nozzle with angle determined uniquely by the local Mach number. Since the fuel nozzle is conical, both direction and Mach number of the flow are not uniform in the core region. This explains why the core boundary is not a straight line, but it is curved inwards. Outside the core region a complex pattern of alternating expansion and compression waves develops and the associated density gradient makes them partially visible. At the free boundary between the jet and the co-flow, the mixing layer quickly becomes unstable and transition to turbulence occurs. In over-expanded conditions the central jet is compressed by the external pressure and its cross section is reduced moving downstream. The extension of the core region is smaller respect to the over-expanded case because of the presence of a conical shock terminating with a Mach disk on the axis as displayed in figure 14c. The strong velocity gradient induced by the Mach disk generates a turbulent wake that grows in size moving further downstream.

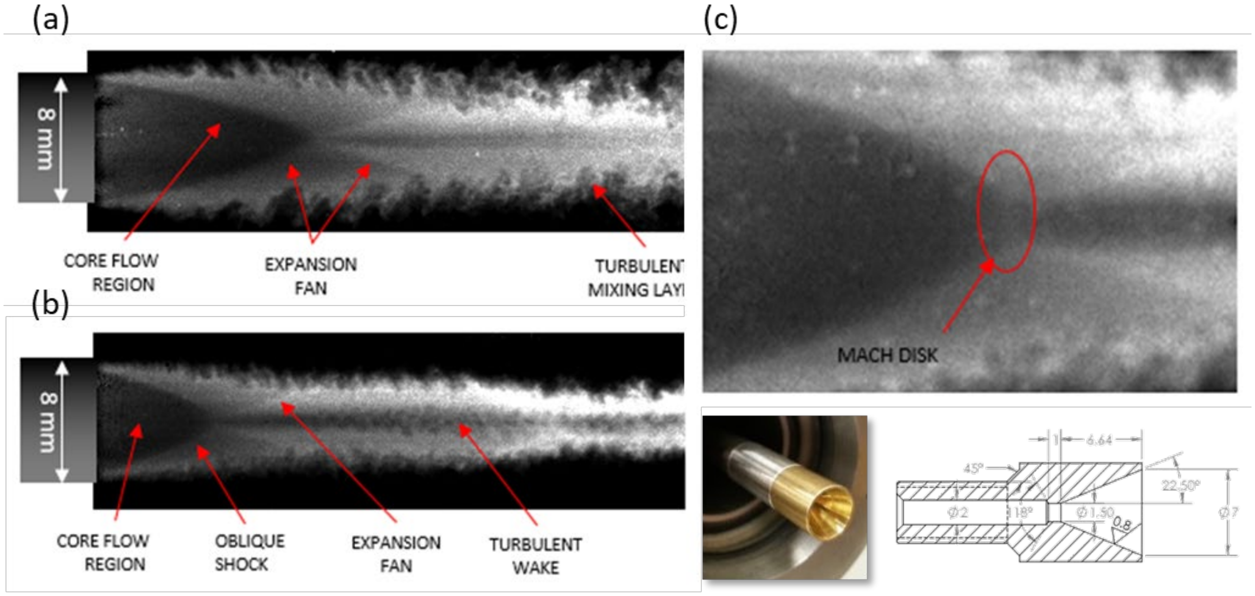

Figure 23. Flow visualization by CO2 PLRS in the direct-connect combustor.

Thermal choking and inlet unstart in a supersonic combustor were investigated in an identical geometry. Inlet unstart is an extremely detrimental event for a supersonic air-breathing engine. When the engine is not able to process the entire airflow captured by the inlet, it spontaneously transitions to a condition in which the incoming flow is compressed by a normal shock standing in front of the inlet. Unstart may be initiated by environmental factors (excessive deceleration of the free-stream, flow distortion, etc.) or by an internal blockage of the engine. The latter mechanism is believed to be caused by a complicated interaction between combustion heat-release, shock waves and boundary layer separation that is still not well understood. The present study is devoted to bridging this gap in our understanding of this phenomena. The long test time allowed by ACT-II along with a simplified circular geometry of the combustor provides a significant advantage over previous similar studies.

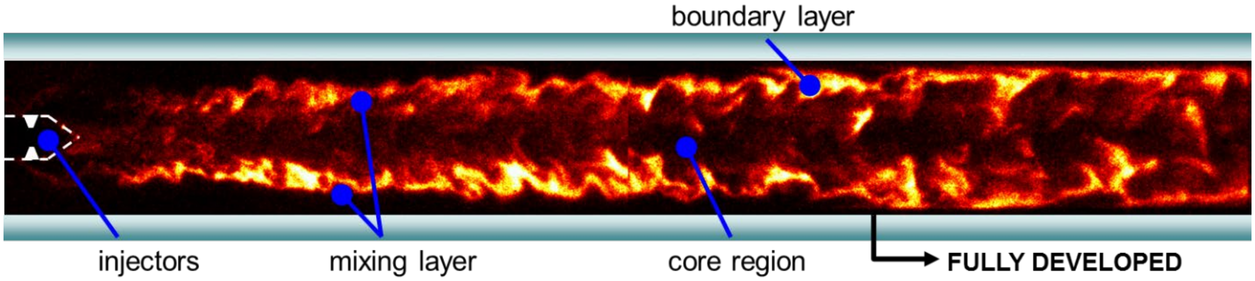

Figure 24. Instantaneous OH PLIF visualization of the combustor in the reacting case. The field of view is 236 × 28 mm. Flow direction is from left to right.

The study revealed that: (1) Combustion (and therefore heat release) occurs mainly inside the turbulent boundary layer, where the residence time is longer, as indicated by OH-PLIF imaging (**Figure 24**). The comparison of heat flux measurements in reacting and non-reacting conditions showed a nearly negligible contribution of combustion heating in the supersonic core. On the other hand, the temperature at the wall, measured by the thermocouples, exhibiting a significant enhancement is the reacting case, due to a warmer boundary layer. (2) Shock train propagation was always initiated by choking of the supersonic flow at the end of the combustor. (3) Choking condition (M=1) is reached mainly through the effects of the irreversibility. This conclusion is supported by the fact that the dependence of the outlet Mach number on the overall total pressure ratio across the combustor is in good agreement with that predicted by Fanno theory.

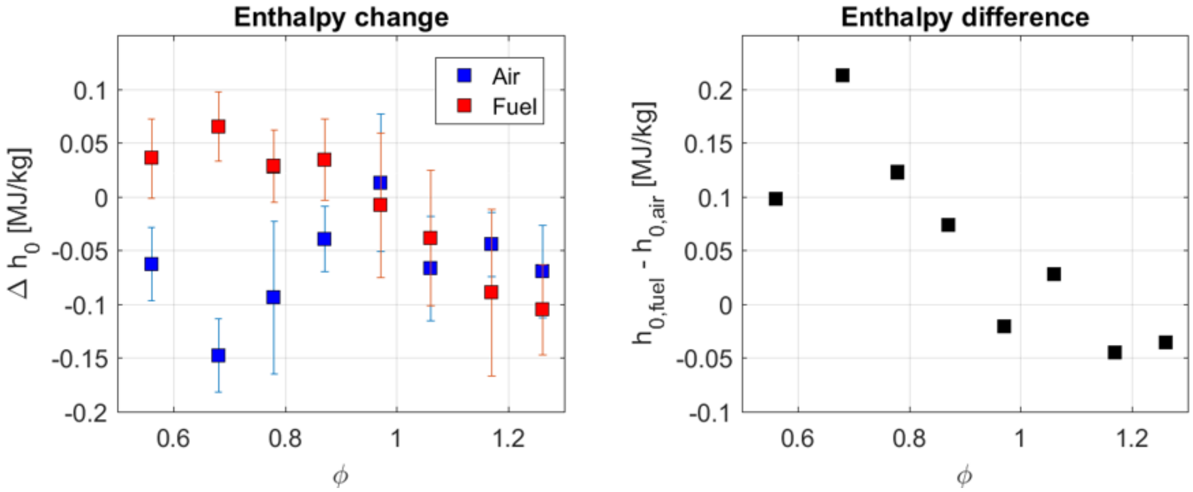

Figure 25. Stagnation enthalpy measurements at the combustor exit.

Figure 25 shows a comparison of enthalpy change in reacting (fuel injection) and non-reacting (air injection) conditions as function of the overall equivalence ratio. The experiments are performed in flow condition A, varying the fuel concentration from $\phi = 0.56$ up to the critical value $\phi = 1.26$. The enthalpy change is measured with respect to the case without injection. The corresponding enthalpy differences between the reacting and the non-reacting cases for each value of ϕ are reported above. A contribution from combustion heat release is observed at lean conditions ($\phi \leq 0.9$) where the reactive mixture yields enthalpies up to 0.22 MJ/kg (corresponding to 10% of the initial stagnation enthalpy of the flow) higher that the non-reacting case. This effect diminishes and ultimately vanishes at higher fuel concentrations, where the measured values are essentially the same for both reactive and non-reactive cases. This behavior can be explained considering that the injected mass of fuel has low temperature and decreases the average temperature of the fuel-air mixture resulting in slower and less efficient combustion. Even close to the incipient choking condition ($\phi = 1.26$) no significant contribution from combustion heat release is observed in the core flow.

Simultaneous measurements of pitot and static pressure at combustor exit have been used to compute the Mach number Rayleigh-Pitot formula

$$\frac{p_{t3}}{p_2}=\left\{\frac{(\gamma+1)^2 M_2^2}{4\gamma M_2^2-2(\gamma-1)}\right\}^{\frac{\gamma}{\gamma-1}}\frac{1-\gamma+2\gamma M_2^2}{\gamma+1}.$$

Above equation relates the ratio between static pressure before (p_2) and stagnation pressure after (p_{t3}) a normal shock to the incoming Mach number M_2. Note that subscript 1 refers to the combustor inlet and subscripts 2 and 3 refer to the location of the measurement respectively before and after a normal shock. Once M_2 is determined, the stagnation pressure before the shock p_{t2} can be calculated by the normal shock relation

$$\frac{p_{t3}}{p_{t2}}=\left\{\frac{(\gamma+1)^2 M_2^2}{2+(\gamma-1)M_2^2}\right\}^{\frac{\gamma}{\gamma-1}}\left\{\frac{\gamma+1}{1-\gamma+2\gamma M_2^2}\right\}^{\frac{1}{\gamma-1}}.$$

Since the stagnation pressure of the flow entering the combustor p_{t1} is measured in the plenum chamber of the tunnel, the overall entropy increase across the combustor can be evaluated by applying the definition and considering that, the stagnation temperature of the core flow does not change significantly.

$$\frac{\Delta s}{R} = \frac{\gamma}{\gamma - 1}\ln\left(\frac{T_{t2}}{T_{t1}}\right) - \ln\left(\frac{p_{t2}}{p_{t1}}\right) \approx -\ln\left(\frac{p_{t2}}{p_{t1}}\right).$$

The local value of γ is affected by vibrational non-equilibrium, air-fuel mixing, combustion efficiency, etc. An accurate estimation of γ is beyond the scope of the present analysis, therefore a representative value $\gamma = 1.31$ is chosen for the entire combustor [Heiser]. **Figure 26** shows a plot of the Mach number at combustor exit as function of the irreversibility computed for unfueled, air-fueled and ethylene-fueled cases. The experimental relation between M_2 and total pressure ratio p_{t2}/p_{t1} across the combustor is in good agreement with prediction of Fanno theory, demonstrating a predominant role of irreversibility in the Mach number reduction process leading to choking.

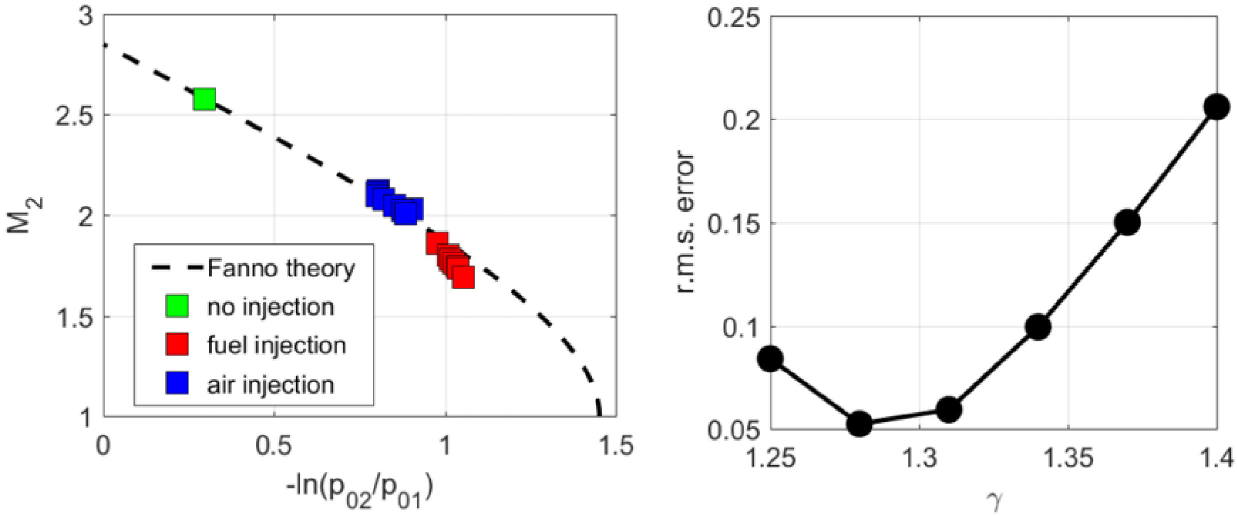

Figure 26. Relation between exit Mach number and total pressure losses determined for pitot pressure measurements and comparison with Fanno theory.

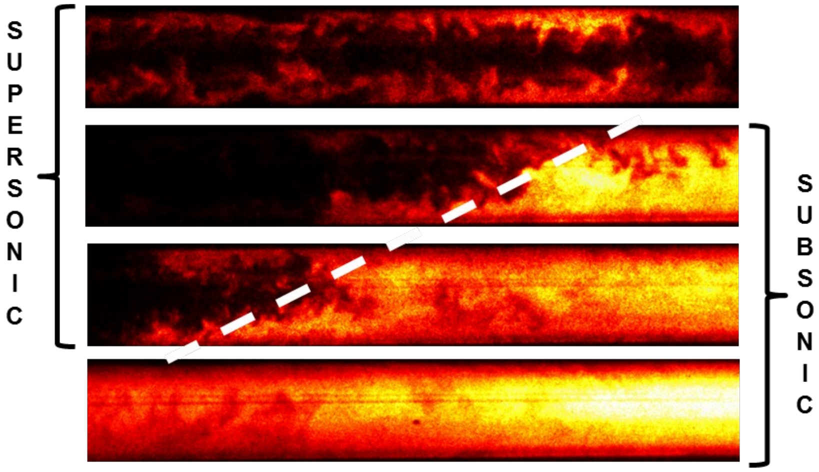

Figure 27. Four stages of pseudo-shock propagation visualized by OH-PLIF.

After choking has occurred an adjustment of the inlet conditions is necessary. The adjustment is accomplished by a train of shocks (pseudo-shock) propagating upstream. The shocks decelerate the flow to subsonic speed with consequent temperature rise. **Figure 27** shows a sequence of the pseudo-shock propagation taken with OH-PLIF. These frames were taken in different tests at the same location, changing the time delay from the start of the propagation. Upstream of the shock, the flow is supersonic and most of the OH is confined inside the boundary layer. Across the shock, due to the reduced speed and higher temperature, the fuel is entirely consumed and the OH (that is a long-living radical) appears nearly uniformly distributed in the central region. Since the wall stays nearly at room temperature during the test, the intensity of the OH signal drops at the wall, where the temperature is lower by the effect of the thermal boundary layer.

2). FREE-JET CIRCULAR CONSTANT-AREA SCRAMJET MODEL

We investigated the pseudo-shock dynamics in the isolator of a free-jet circular scramjet model in low enthalpy conditions, as shown in **Figure 28**. The model is composed by a conical inlet (area ratio 1.3-1.9) a 200 mm isolator a 300 mm combustor (both 35 mm I.D.) and a nozzle. The fuel is injected through 4 radial jets located between isolator and combustor. In the first part of the work, the isolator flow was visualized using planar laser Rayleigh scattering (PLRS) of condensed CO_2 particles. Pure CO_2 at Mach 4 was used for the free-stream and choking was induced by injection of nitrogen at high pressure through the fuel ports. For mass injection rates above 13%, onset of oscillations is observed in the isolator.

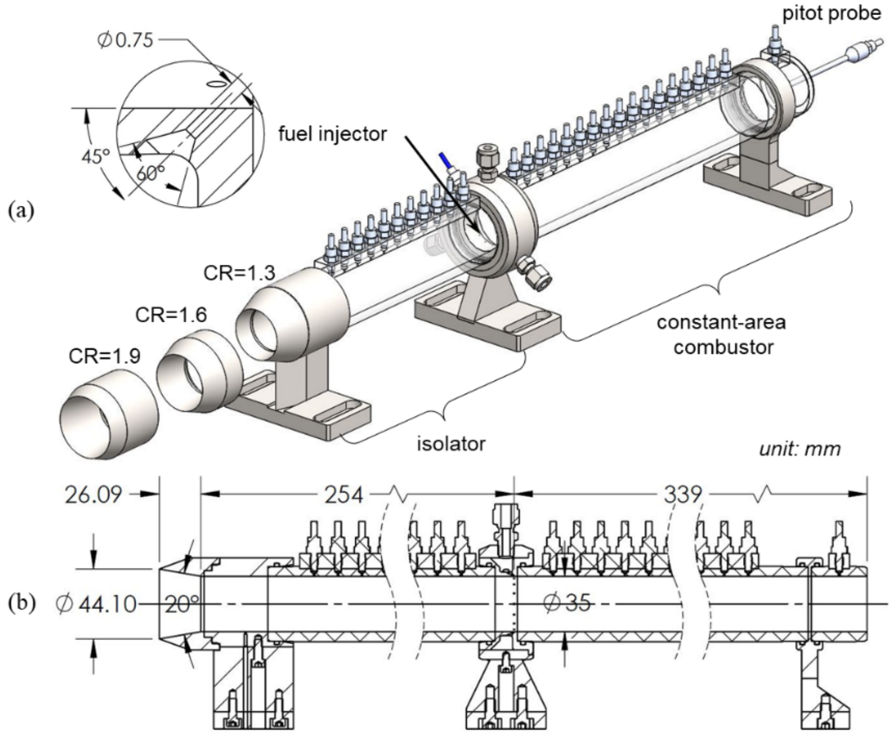

Figure 28. An overview of the scramjet model with three inlet options. (b) Dimensions of the model with the inlet CR=1.6.

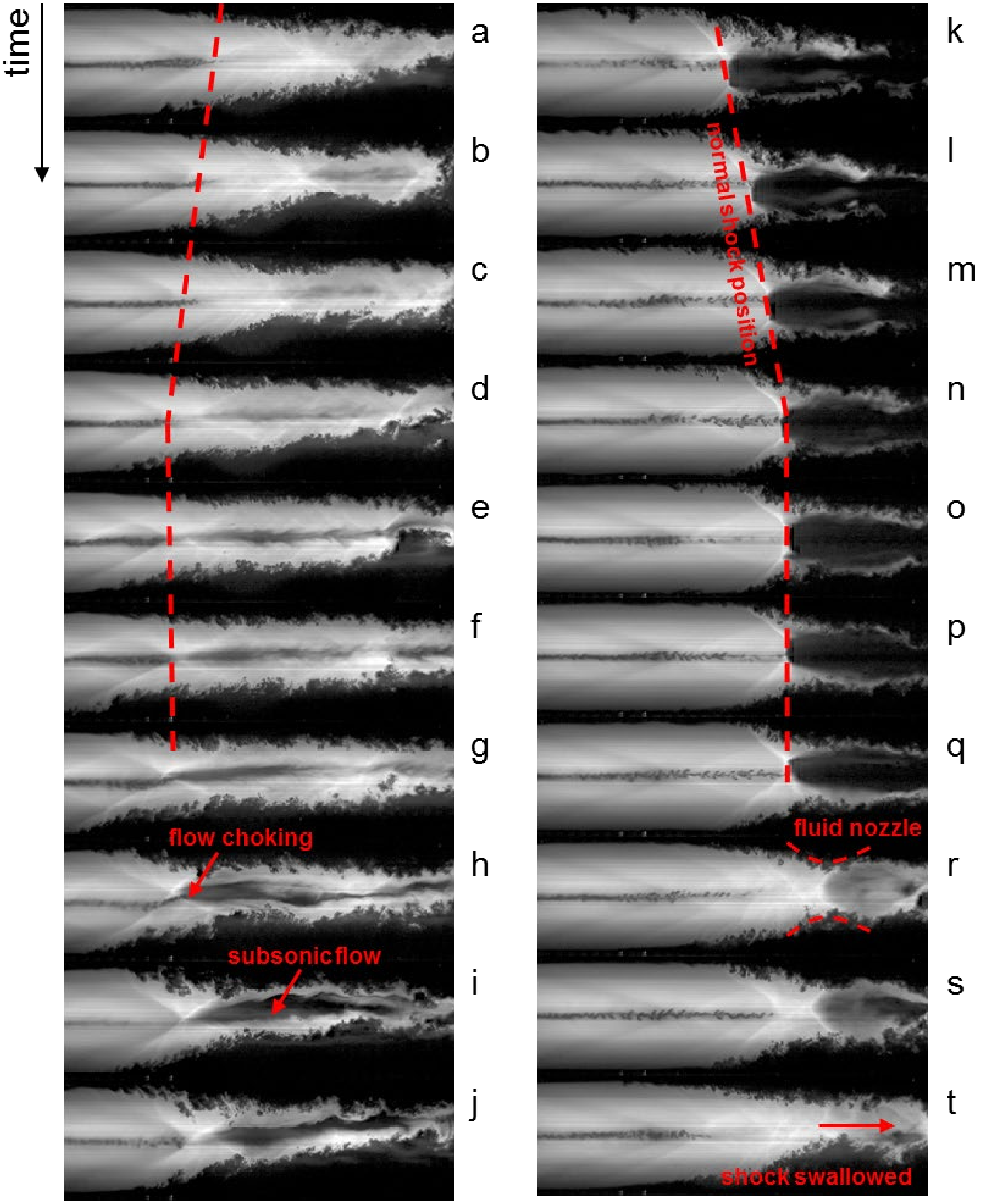

Figure 29. PLRS visualization of the isolator flow. Flow direction is from left to right. The pseudo-shock propagates upstream in the left column and downstream in the right column. Time interval between the frames not constant.

Figure 29 shows the PLRS visualization of the isolator flow. Flow direction is from left to right. The pseudo-shock propagates upstream in the left column and downstream in the right column. Time interval between the frames not constant. As the shock is stretched, the size of the separated boundary layer grows, confining the supersonic core to a progressively smaller area. Ultimately (*h*), the blockage effect becomes strong enough to choke the flow.

A shock wave propagates upstream up to the inlet. A normal shock is formed close to the centerline and a large portion of subsonic flow is created downstream (*i* and *j*). During the downstream propagation (k to *q*), about 2.0 ms long, the pseudo-shock collapses to a bifurcated single normal shock. The pressure distribution across the normal shock shapes the separated region as a converging diverging channel that opposes to the further advancement of the shock. Finally, the shock is swallowed through the throat (*r* and *s*) and the flow re-accelerates to supersonic speed (*t*). The entire process is completed in about 2.5 ms, corresponding to a frequency of 400 Hz. There cross sectional images of the pseudo shock wave are unique and unprecedented in the study of flow choking in any configuration.

3). CAVITY FLAMEHOLDING IN AN AXISYMMETRIC SCRAMJET

The stabilization of hydrocarbon combustion reactions in scramjets has been one of the most critical issues in developing the next generation of air-breathing propulsion systems [Hesier]. The ignition, flame holding and combustion stabilization for hydrocarbon fuels are challenging in scramjet combustors because the characteristic reaction time scales of hydrocarbon fuels tend to be longer than the supersonic flow residence time, though hydrocarbon fuels have been candidates for scramjet propulsion due to their high energy density, general availability and easier handling [Segal].

Cavity flameholders have long been used as integrated fuel injection/flame-holding approaches for supersonic flame stabilization and combustion performance improvement in scramjet engines due to their minimal system complexity and performance detriment (i.e., total pressure losses) [Gruber]. Wall cavities in scramjet combustors can increase flow residence time and enhance fuel/air mixing rate by creating recirculation regions and pools of hot radicals that reduce the induction time of chemical reactions and serve as self-sustaining ignition sources [Ben-Yakar]. The cavity flame-holding phenomena have been widely studied with various fueling schemes and mixing enhancement strategies in rectangular direct-connect supersonic combustors [Mathur,Rasmussen,Tian] and rectangular scramjet models [Jeong].

However, flow separations induced by corner boundary-layer effects can introduce significant flow distortions, unsteady flow and shockwave behaviors in rectangular scramjets, causing unpredictable flame propagation behaviors and affecting the physicochemical phenomena in cavity flameholders and supersonic combustors. Yentsch et al. [Yentsch] investigated the mode-transition phenomena in a rectangular scramjet and its equivalent axisymmetric scramjet via numerical simulation, and found that the boundary layer separation from corner flow effects in the rectangular geometry dominated the flame-holding transition from primary injector zone to secondary injector zone in scramjet dual-mode operation, while the lack of forward flow separation in the axisymmetric configuration emphasized the mode transition as the weak combustion in the primary combustor disappeared and localized near the downstream injectors. Therefore, the investigation of cavity flame-holding phenomena including the overall flow dynamics and flame propagation in scramjet combustors demands for flowpath configurations with the elimination or reduction of corner boundary-layer effects, i.e., elliptic or axisymmetric scramjets.

Increasing interests have been aroused to explore the benefits in operability with elliptic and axisymmetric scramjet combustors [Smart,Denman,Gruber,Billig,Riggins,Yao]. The benefits of such scramjet combustors compared with rectangular combustors include undesirable effects from the hypersonic corner boundary-layer effects, the increased structural efficiency, decreased structural weight required to withstand a specified pressure/thermal load and the reduced wetted surface area needed to enclose a specific cross-sectional area. Gruber et al. [Gruber] characterized the flowpaths of a hydrocarbon-fueled axisymmetric scramjet combustor with a wide operation range in a direct-connect supersonic combustion facility. Smart and Trexler [Samrt] proposed a hypersonic inlet with rectangular-to-elliptical shape transition (REST) and tested the inlet performance in combination with an elliptical combustor. Denman et al. [Denman] investigated the supersonic combustion of hydrocarbon fuels and cavity flame-holding ability inside the scramjet with REST inlet at Mach 8 flight conditions. Due to intrinsic limitations from complicated curved surface design/fabrication and test facility operation conditions, optical accesses into the elliptical or axisymmetric scramjet models have remained a significant challenge though it is necessary for investigation on internal flow and combustion dynamics in combustors.

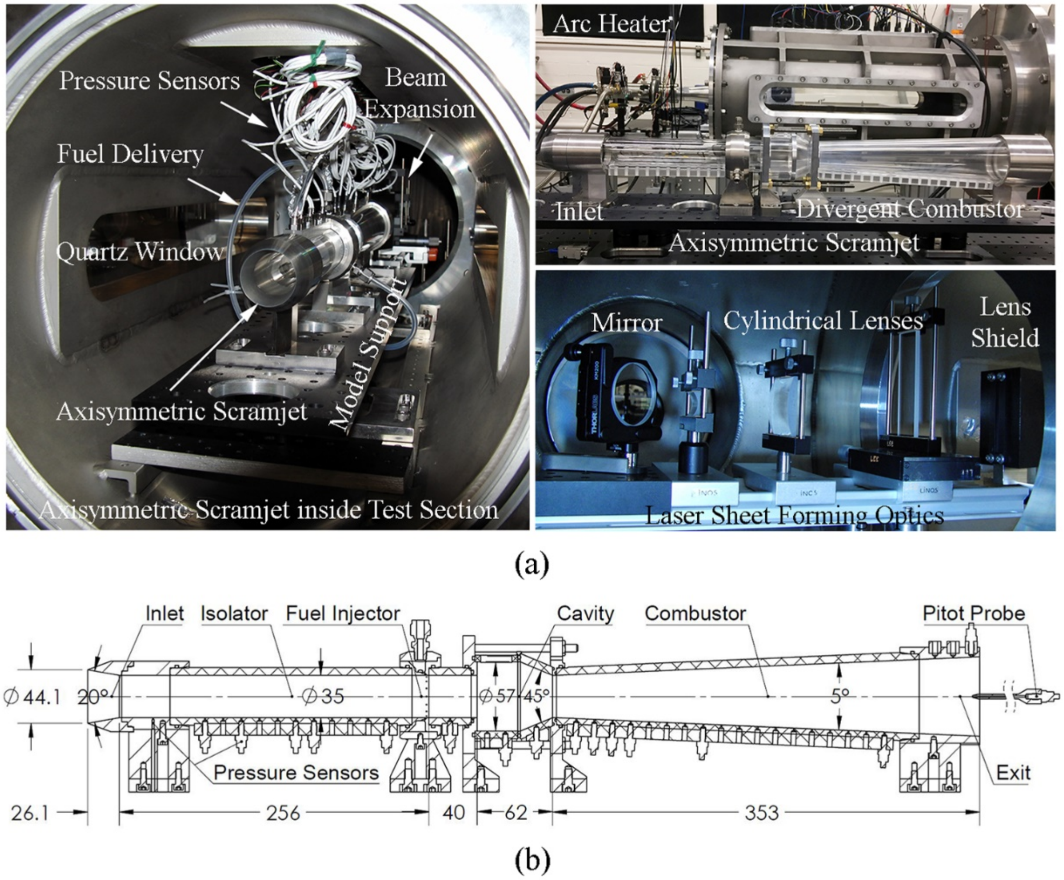

Figure 30. (a) Photographs of an experimental facility and (b) schematic of an axisymmetric scramjet (units in mm).

In this study, a simplified and generic axisymmetric scramjet model with optical access is designed for fundamental studies on flow and combustion dynamics and tested at Mach 4.5 flight conditions. The cavity flame-holding phenomenon in the axisymmetric scramjet fueled with ethylene is investigated experimentally. Flame visualization using hydroxyl (OH) planar laser induced fluorescence (PLIF) technique and static pressure measurements are accessible for the entire combustor flowpath which is novel. Flow and combustion dynamics are studied in both axisymmetric scramjets with and without the cavity flameholder to verify the cavity flame-holding ability. An axisymmetric scramjet is installed in the open-type test section of ACT-II facility as shown in **Figure 30**. The axisymmetric scramjet model uses modular design and the cavity flameholder can be replaced by a constant cross section tube with the same diameter of isolator.

The ethylene flame dynamics and the flame structure in the model scramjet are observed using an OH-PLIF imaging system through the ultra-violet (UV) transmitting acrylic tubes of the model scramjet.

Table 1 Experimental conditions.

Case	Cavity	Freestream P_0	Freestream T_0	Fuel Injection Injectant	Fuel Injection Mass flow	Fuel Injection Overall ϕ
		kPa	K	-	g/s	-
1	Yes	161.4	2206	-	0	-
2	Yes	164.2	2181	Air	0.94	-
3	Yes	164.5	2204	Ethylene	0.58	0.64
4	Yes	164.7	2196	Ethylene	0.96	1.06
5	Yes	164.4	2180	Ethylene	1.41	1.56
6	No	163.7	2235	-	0	-
7	No	163.4	2226	Air	0.97	-
8	No	163.9	2203	Ethylene	0.58	0.65
9	No	164.9	2217	Ethylene	0.98	1.10
10	No	163.8	2197	Ethylene	1.43	1.59

Flame visualization using OH PLIF has been achieved in an optical axisymmetric scramjet at ethylene-fueled conditions for the first time and the axisymmetric cavity flameholder is characterized at various fueling rates to investigate the flameholding ability via flame distribution and pressure measurement. Experimental conditions are summarized in **Table 1**. **Figure 31** shows the OH PLIF images with the presence/absence of a cavity at three nominal overall equivalence ratios, $\phi = 0.65$, 1.10 and 1.60 at flow conditions of $T_0 = 2200$ K, $P_0 = 1.6$ bar. **Figure 32** shows the corresponding pressure distributions with/without a cavity at various fueling conditions.

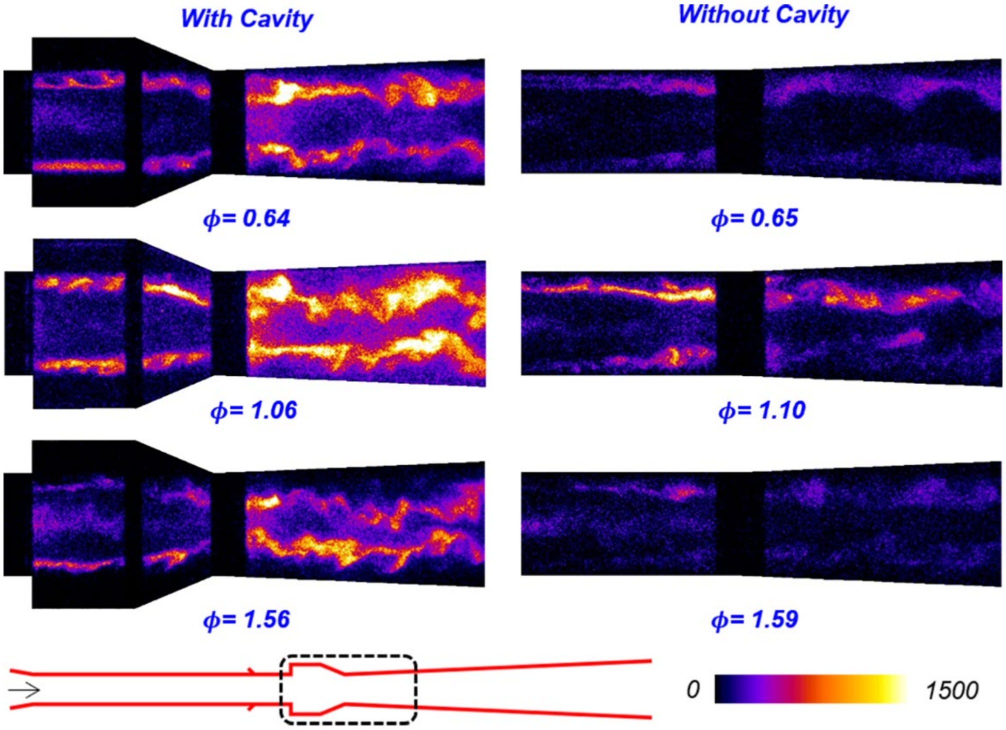

Figure 31. OH-PLIF images in ethylene-fueled experiments.

Cavity flameholding is achieved at a wide range of fueling conditions as seen by the direct comparison of OH PLIF images and pressures between the configurations with cavity (Cases 3-5) and without cavity (Cases 8-10). Both the pixel intensities of OH fluorescence images and areas of flame distribution with the cavity flameholder are apparently larger than without the cavity, as seen in **Figure 31**. In Cases 3-5 with the cavity, the flames are auto ignited and distributed along the shear layer piloting the combustion inside the divergent combustor, while the flame structures evolve with the flowpath from laminar-like flame fronts to highly distorted flame fronts. In contrast, at near stoichiometric fueling conditions (Cases 8-10), most of the flame intensities are barely observable except for a thin layer of strong combustion that exists before flow expansion through the divergent combustor. Therefore, the heat release rate and combustion efficiency are low with the absence of a cavity. This observation is further confirmed by comparing the pressure distribution of Case 4 with that of Case 9 at stoichiometric fueling condition. The pressures are lower near the jet injection region but higher in all the divergent combustor region in Case 4 with cavity than in Case 9 without cavity (**Figure 32**a). This is because the jet-induced bow shocks in Case 9 impinge on the solid wall and flow separations move upstream, driven by high back pressure up until the jet wake region (**Figure 32**c). In Case 4, bow shocks caused by jet injection impinge into the cavity volume and no apparent pressure rises are observed in the region upstream of the cavity (**Figure 32**b). However, significant pressure rises are observed at the cavity ramp and divergent combustor entrance at all fueling conditions due to shear layer impingement onto the ramp and combustion heat addition as well as mass loading (**Figure 32**a and **Figure 32**b). The pressures over the divergent combustor in Case 4 are higher than that in Case 9 despite the total pressure losses from combustion heat addition and shock interactions with the presence of a cavity. The comparison between Case 2 with air fueling and Case 4 with ethylene fueling at the same mass flow rate presents the same tendency, i.e., the increased pressure rises inside the divergent combustor with a cavity is due to the combustion heat release rather than possible reduced pressure losses from fluid dynamics. Therefore, combustion stabilization and flameholding are well established by the cavity. It is noteworthy the instantaneous flame structures were not observable inside the cavity volume due to the limitation of laser sheet projection arrangement in this study. A laser arrangement able to entirely cover the cavity volume is currently under design, and it will be implemented in the continuation of this activity.

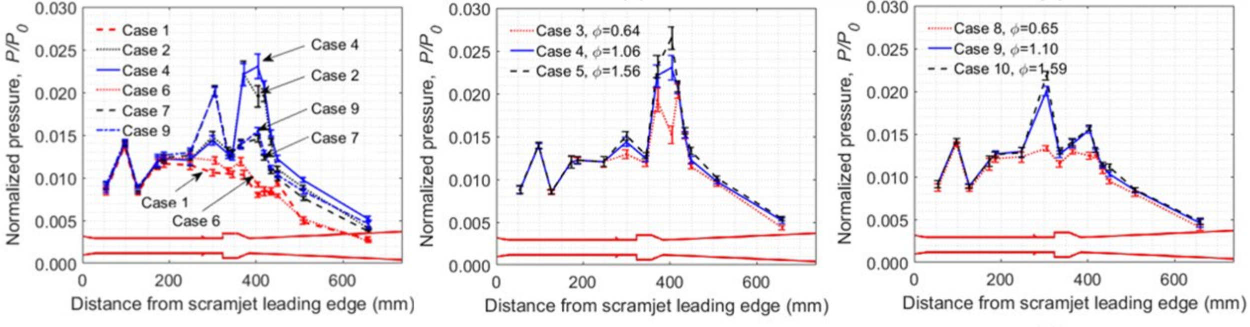

(a) (b) (c)

Figure 32. Pressure distributions at (a) unfueling, air-fueling and stoichiometric fueling conditions with and without a cavity, (b) various fueling rates with cavity, (c) various fueling rates without cavity.

In this experimental configuration, the flame front transition enhanced by the shear layer development takes a dominant role in combustion stabilization process. The supersonic flame is auto ignited by a jet induced bow shock rather than forced ignition by a spark inside a cavity, and the flame elongates from the jet plume along the flowpath and passes by the cavity while perturbed and stabilized by the shear layer development. The laminar-like flame front transforms to corrugated flame structures while passing by the cavity leading edge where the shear layer grows and tends to be unstable at all three fueling conditions. The corrugated flame fronts are thin and continuous at fueling condition ϕ=0.64 whereas the flames have increased length scales with thick and saw-like fronts at fueling condition ϕ=1.06. These phenomena have rarely been observed in cavity flameholding studies in freestreams with low total temperatures (T_0 < 1300 K) that fuel autoignition cannot be achieved. In these studies, the combustion inside a cavity is initiated by a forced ignition system and intense flames are stabilized in the shear layer region and spread into the main stream at a certain angle with the flame base anchored at a location where the flame speed equals the flow convection speed after the cavity leading edge. Once the flame is auto ignited in high-enthalpy freestreams (T_0 > 2000 K) upstream of the cavity flameholder, the flame tends to be distributed above the cavity flameholder and stabilized along the shear layer whereas no apparent flame spreading angles are observed. These phenomena are consistent with the observation in this study. In these two ignition schemes, the flow temperature is higher compared to fuel ignition temperature in mainstream above the shear layer in autoignition cases with high-enthalpy freestreams whereas the situation is reversed in forced ignition cases with low-enthalpy freestreams. Therefore, the flame stabilization mechanisms inside cavity volumes and shear layer regions are different considering the shear layer boundary conditions and needs to be further investigated.

The cavity flameholding benefits not only from the creation of flow recirculation regions and continuous radical additions into flows that reduce the combustion induction times but also from the shock-attended interactions caused by the presence of a cavity. In this cavity configuration, a circular recompression shock develops at the cavity ramp and impinges on the divergent combustor wall. It is clearly seen that the flames downstream of the cavity are significantly distorted and localized as indicated by pockets of intense combustion regions connecting with thin flame interfaces. Nevertheless, the dominant factor for flame stabilization downstream of the cavity, continuous hot radicals supply or shock interactions, remains undetermined. The general contribution from the cavity and the combustion heat addition can be visualized by the Mach number measurement at the combustor exit. The Mach number profiles in the radial direction at the combustor exit plane are presented in **Figure 33**. At the combustor exit, the average value of heat capacity heat ratio γ is 1.31 to model the properties of the real fuel/air/combustion products mixture. The Mach numbers are calculated using the Pitot-Rayleigh formula assuming a negligible radial pressure gradient. In Cases 1 and 6 without the jet injection condition, the cavity produces stronger shockwaves that decelerate the flow mainly in the core flow region. Any jet injection will introduce excessive shock losses that further reduce the flow Mach number at the combustor exit with and without a cavity, as seen in Cases 2 and 7. In Cases 2 and 4 with the cavity flameholder, the Mach number remains the same in the combustor center (the same shock loss in the core flow), and the impact of heat addition mainly decelerates the flow Mach number at regions beyond 10

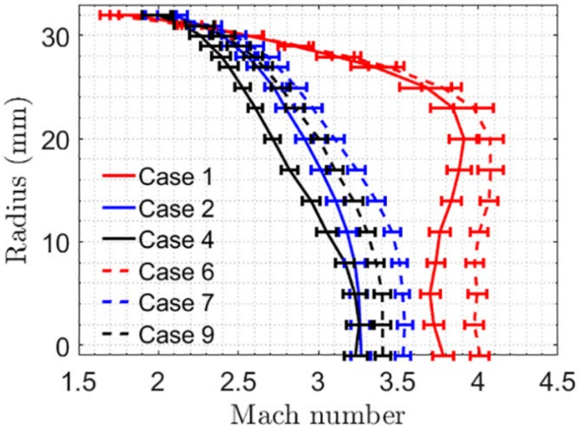

Figure 33. Mach number distributions in the radial direction at the combustor exit.

mm radius. In Cases 4 and 9 without the cavity, the impact of heat addition is relatively mild, and the overall Mach number is higher than that in cases with a cavity. Hence, the heat addition from cavity-stabilized flames contributes more in the near-wall region than the core flow region. Flow deceleration in the core flow region is mainly from shock losses and weakly connected to the combustion heat addition (i.e., heat transfer from the near-wall region to the supersonic core).

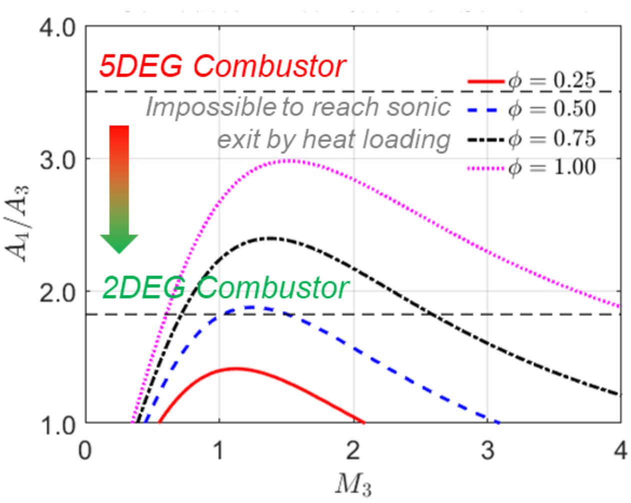

Figure 34. Scramjet operational diagram with the sonic condition at combustor exit.

Although the cavity flameholder reduces the combustion induction time and improves the overall flow mixing, proper combustor area relief is necessary to optimize the combustion heat addition process and stabilize the flame downstream of the cavity flameholder, i.e., to maximize the combustion efficiency to obtain the potential performance of scramjet engines. Billig [Billig] defined the optimal heat addition process in scramjet combustor based on pressure-area relationship, i.e., the least entropy rise for a give stagnation temperature rise and set of initial conditions, which can be realized for the case of sonic condition at combustor exit. The combustion efficiency can be enhanced by improving the fuel-air mixing rate, flow residence time, static pressure/temperature of supersonic flows in the combustor that decrease the Mach number along the flowpath in supersonic flow regime.

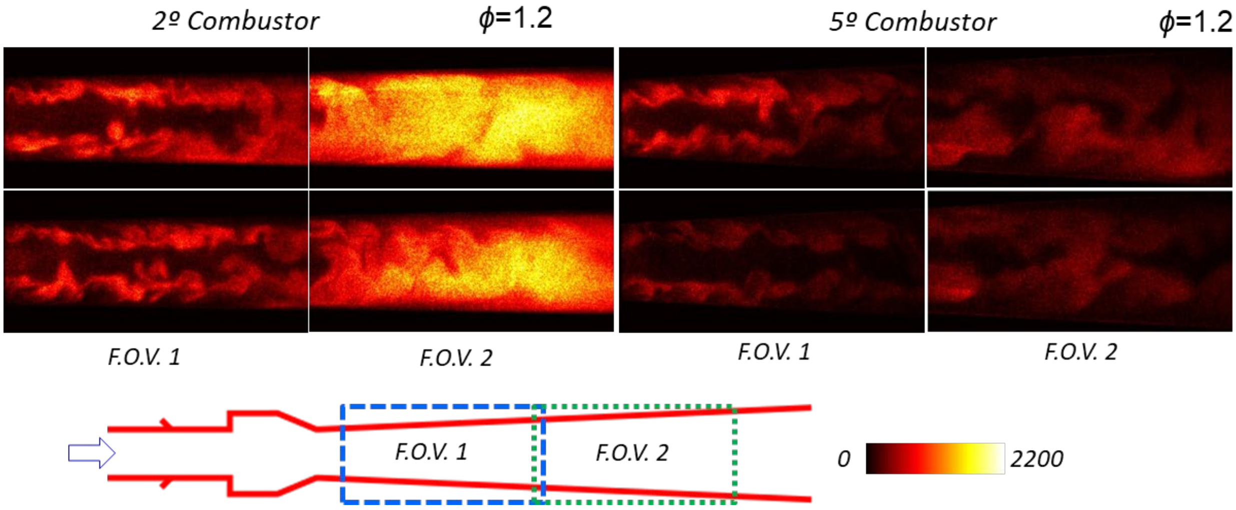

Figure 35. OH-PLIF images of steady-state flames at 2-deg and 5-deg diverging combustors.

Combustor performance analysis shown in **Figure 34** indicates that there exists no solution for the 5-deg combustor to choke at the combustor exit at any given combustor entry Mach number and ideal combustion heat addition rate at equivalent fully premixed equivalence ratio. Theoretically, the 5-deg combustor with current length cannot be choked by combustion heat loading at current flow total enthalpy condition. The experimental observation confirms the theoretical prediction and evidences the potential choking location for scramjet combustor with cavity flameholding and excessive area relief, i.e., the cavity region. In addition, the diverging combustor with excessive area relief tends to have fast Mach number increase and static temperature/pressure drop along a short flowpath, which will potentially quench or freeze the ongoing high-temperature combustion reactions. **Figure 35** shows the OH PLIF images taken at the fuel mass flow rate of 0.45 g/s with different diverging combustors. The intensities of hydroxyl fluorescence signal are comparable immediately downstream of the cavity region for 2-deg and 5-deg combustors; the pixel intensity in 2-deg combustor increases mildly along the flowpath while the pixel intensity quenches apparently in 5-deg combustor.

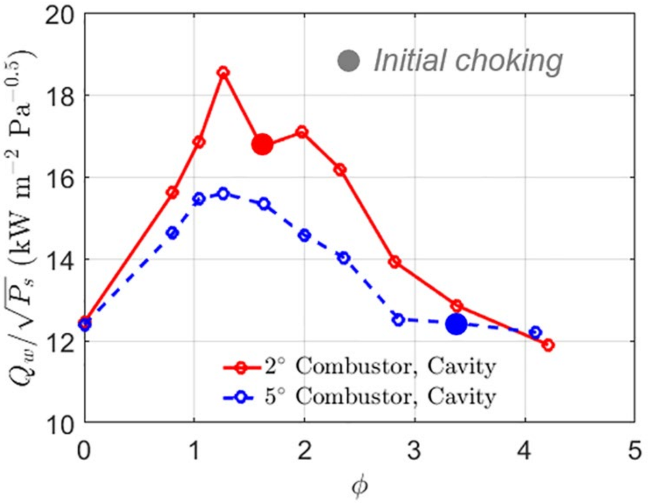

Figure 36. Normalized heat flux measurements with 2-deg and 5-deg diverging combustors.

The combustion in 2-deg combustor is more efficient than that in 5-deg combustor in this study. As shown in **Figure 36**, the 2-deg diverging combustor choking at a smaller ϕ compared to the 5-deg diverging combustor. Interestingly, the 5-deg combustor does not choke at its peak combustion heat addition into the supersonic flow but at extremely impractical high fuel loading when its combustion efficiency and heat addition into the core flow are low. The pressure contours in *x-t* plane indicate the initial choking location as shown in **Figure 37**, the choking occurs in the diverging combustor section and propagates upstream until the cavity flameholder in the 2-deg combustor, while the choking occurs inside the cavity region (close to the ramp side) and no flame propagation is observed in the 5-deg combustor. Therefore, the choking event and unsteady flame propagation in 2-deg combustor are mainly induced by excessive heat addition into the core flow as indicated by the heat flux measurement; in contrast, the choking event in 5-deg combustor mainly results from excessive total pressure losses from extremely strong jet-induced bow shockwaves and recompression shock at cavity ramp, which decreases the Mach number in the supersonic core inside the cavity region, rather than combustion heat addition in the diverging section. Given the same fuel mass flow rate below the choking limit and flow conditions at the isolator exit (i.e., combustor entry), the Mach number at combustor exit is much higher than one for the 5-deg combustor than that for 2-deg combustor, i.e., the combustion process in the 2-deg combustor with a cavity flameholder is closer to the optimal process. It is noteworthy that the unsteady flow dynamics occurring in the cavity and diverging combustor section results from the pseudo shock dynamics during the inlet-isolator-combustor interaction.

The axisymmetric scramjet with a cavity flameholder and a diverging combustor (cone angle 2 deg) is experimentally investigated with: (1) no fueling, (2) air injection and (3) ethylene injection at various fueling rates. Parallel experiments are carried out at the same fueling schemes with the cavity flameholder replaced by a constant cross-section tube. **Figure 38** presents the pressure distributions along the flowpath downstream of the fuel injection port in scramjet combustor configurations with and without a cavity flameholder.

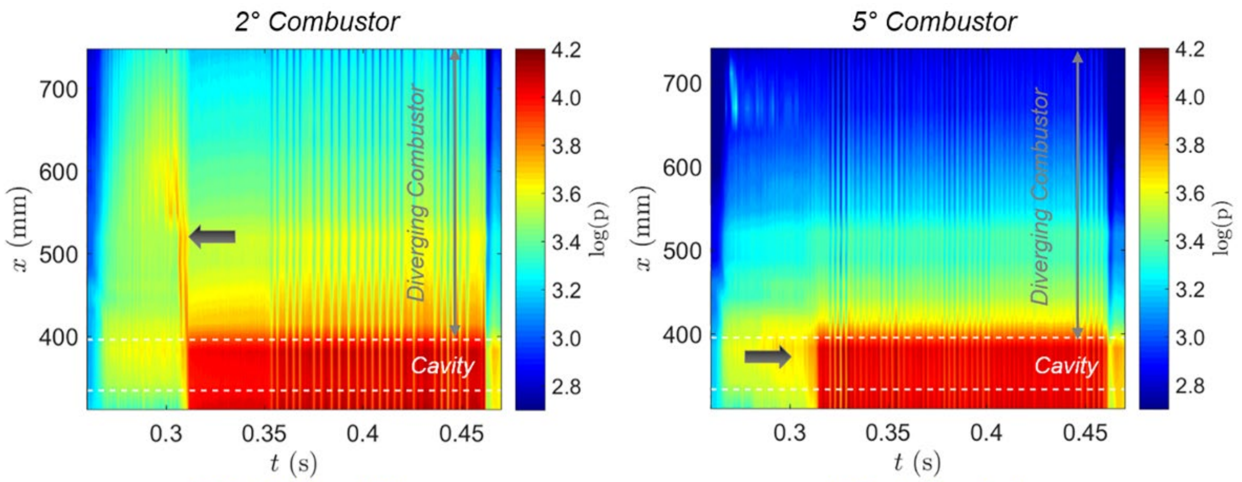

0.89 g/s (*ϕ* = 1.7)

1.80 g/s (*ϕ* = 3.4)

Figure 37. Pressure contours in an x-t plane at choking limit.

The combustion stabilization in a generic 2-deg diverging combustor configuration has been achieved by the cavity flameholder as indicated by comparisons between the pressure distributions with and without a cavity. With an axisymmetric cavity flameholder, the pressure profiles have a peak (local maxima) in the cavity ramp region and another peak in the diverging combustor region. The first pressure peak at the cavity ramp results from the shear layer impingement on the cavity ramp while the second peak originates from the combustion heat addition. In supersonic flows, the combustion heat addition decreases the flow Mach number while the area relief increases the flow Mach number; whether the Mach number decreases or increases depending on the combined effects from the combustion heat addition rate and the combustor area relief. The static pressure increases with the decreasing Mach number along with the flow path. The ordinary differential equation of the static pressure without the wall friction term for constant specific heat and molecular weight term from Shapiro [Shapiro] is

$$\frac{dP}{P} = \frac{\gamma M^2}{1-M^2}\left[\frac{dA}{A} - \left(1+\frac{\gamma-1}{2}M^2\right)\frac{dT_t}{T_t}\right].$$

where P is the static pressure, M is the Mach number, A is the combustor cross-section area, and T_t is the flow total temperature. For $M>1$, the combustion heat addition dominating the process leads to $dP/P>0$, *i.e.*, $\left[1+(\gamma-1)M^2/2\right]dT_t/T_t > dA/A$, as evidenced by the pressure distribution shown at x = 450-600 mm in **Figure 38**a with ethylene mass flow rate of 0.69 g/s. The local maximum pressure value increases with the fueling rate (0.44-0.69 g/s) results from the increased combustion heat addition while the combustor geometry is unchanged. Downstream of the local pressure maxima in the diverging combustor, most of the injected fuel has been consumed in combustion and the combustor area relief dominates the aerodynamic process. The area expansion increases the flow Mach number in the supersonic core and decreases the static pressure along the flowpath. The combustor downstream of the maximum pressure location behaves as an expansion section at x > 650 mm. In contrast, these phenomena are not observed in the combustion configuration without a cavity flameholder shown in **Figure 38**b. The cavity flameholder can enhance the supersonic combustor performance by promoting the fuel-air mixing, enhancing heat transfer rate from the boundary flow region to the supersonic core, and reducing the combustion induction time by flow preheating and potential radical supply to flow downstream from flow recirculation region in the cavity. Due to the lack of such mechanisms for combustion enhancement in flow configuration without a cavity, the combustion heat addition in the diverging combustor is not sufficient to compete with the area relief effect, which results in the continuous pressure drop along the flowpath. In addition, the pressure distributions are not sensitive to the fuel mass flow rate due to the insufficient fuel-air mixing as shown in **Figure 38**b.

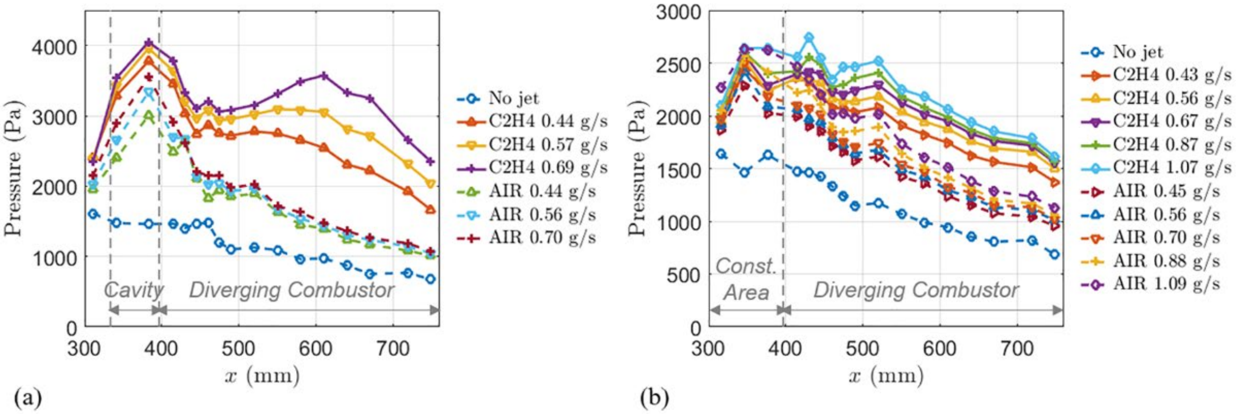

Figure 38. Pressure distributions in a model scramjet with a) a cavity flameholder, and b) a constant-area flow channel.

As the aerodynamic parameters of supersonic core flow in the diverging combustor determine the critical operating condition leading to the flow choking and scramjet operational mode transition, quantitative heat flux and total pressure measurements are conducted in the supersonic core flow at the combustor exit to assess the combustor performance enhanced by the cavity flameholder.

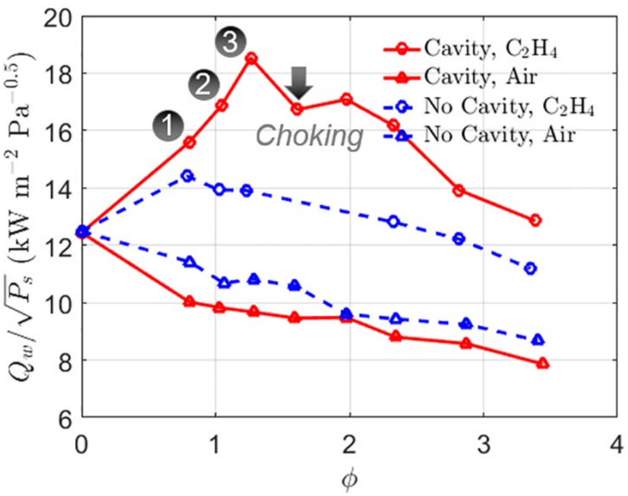

Figure 39. Simulated excitation spectra for OH and CH with custom filter stack transmission properties.

Figure 39 shows the heat flux measurements at the stagnant point after a normal shock in various ethylene fueling rates. The normalized heat flux is linearly related to the total flow enthalpy and hence an explicit indicator of the combustion heat addition. It is clearly observed that the pressure rises in the diverging combustor result from the combustion heat release. With the cavity, the normalized heat flux increases by 50% with the increase of the fueling rate until the flow is choked at $\phi = 1.6$ and above. With the air injection, the total flow enthalpy decreases with the air mass flow rate due to the cooling effect of the room-temperature air. The normalized heat flux with air injection is approximately half of that with ethylene injection at equivalent $\phi = 1.3$. Interestingly, the cooling effect from air injection is more apparent with a cavity flameholder compared to that without a cavity. As the cavity enhances the injectant-freestream mixing, the heat transfer from the supersonic core to the cold injectant is more efficient and the flow enthalpy in the core flow is lower.

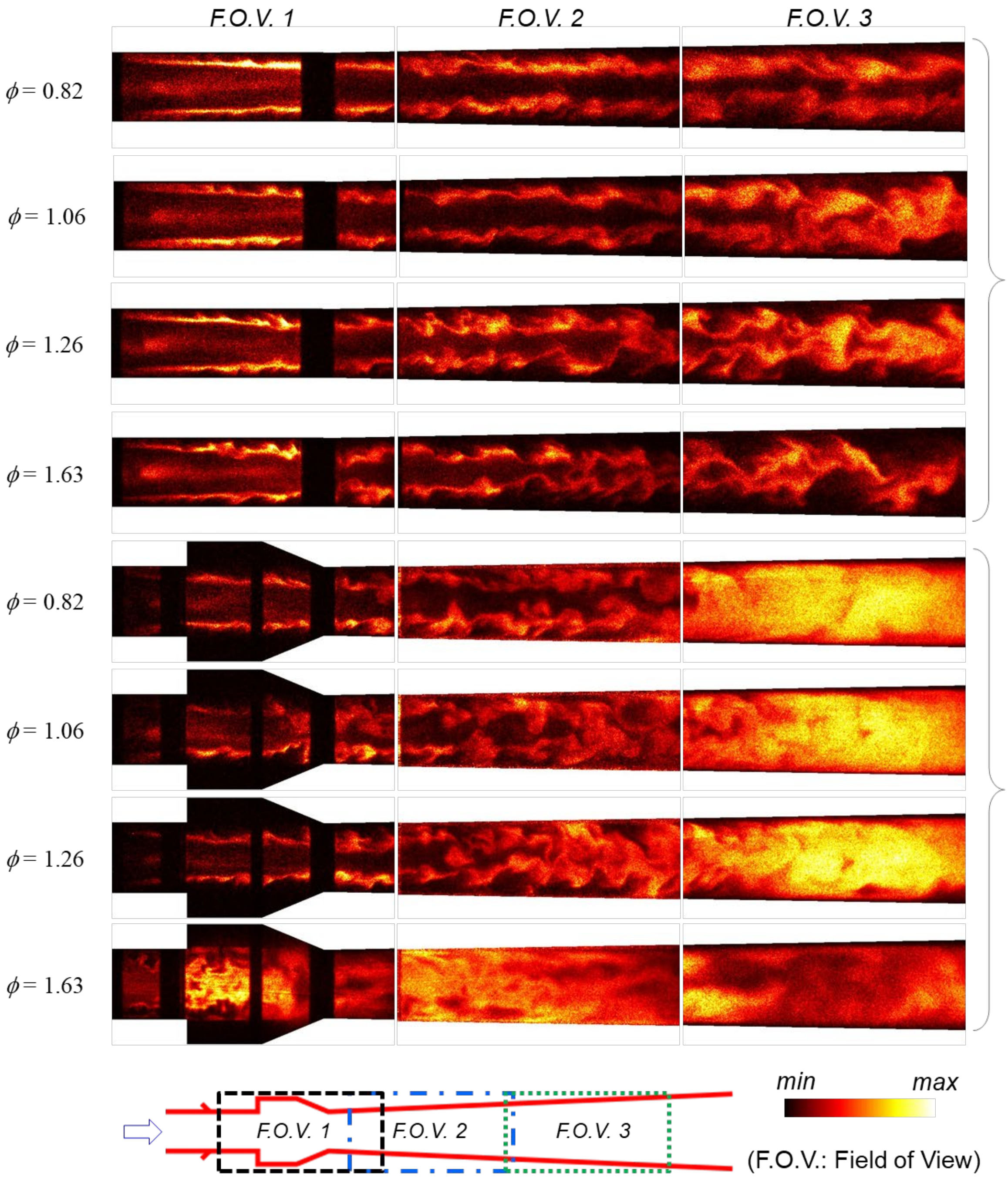

Figure 40. OH-PLIF images of steady-state flames in 2-deg diverging combustor.

Resolving detail flame structures and distributions are necessary to further understand the cavity influences on combustion dynamics although the cavity enhances the overall combustion and impacts the combustor performance as quantified by static pressure measurement on the combustor wall, total pressure and heat flux measurements at the combustor exit. **Figure 40** shows the flame structures at steady state are resolved using OH PLIF imaging in three fields of views (F.O.V.) with/without a cavity flameholder at various ethylene fueling rates.

It is observed that the cavity promotes the transition of laminar-like flame fronts to large-scale flame structures and direct the fuel into the core of the flow in the diverging combustor.

Without a cavity flameholder, a laminar flame structure is sustained over a longer distance in the constant area combustordownstream of the fuel injection before the transition to large-scale turbulent flames. The increased ethylene fueling rate promotes the flame front transition process inside the constant-area section. With the presence of a cavity, the flame fronts are perturbed immediately from the cavity leading edge due to expansion waves and shockwaves introduced by the cavity. The fuel-air mixing near/above the shear layer originating from the cavity leading edge is further enhanced by the shear layer instability and the shockwave-shear layer interactions. At the cavity trailing edge, a recompression shockwave developed above the cavity ramp deflects the fuel-air mixtures/shear layer toward the core of the flow, which cannot be observed in the configuration without a cavity. The large-scale flame structures enhance the fuel-air mixing processes by entraining massive oxidizers into fuels, stretching fuel-air interfaces, increasing the interfacial areas, and/or steepening the local concentration gradients in molecular diffusion processes [Gruber, Ben-Yakar]. As shown in **Figure 40**, the hydroxyl radicals indicating the ongoing high-temperature combustion reactions fill the combustor core in the most downstream field of view at $\phi = 1.26$ without a cavity. In contrast, the intense combustion spreads over the entire combustor volume downstream even at fuel lean condition $\phi = 0.82$ with a cavity in this study. These observations are consistent with the quantitative measurements using pressure transducers and heat flux probe.

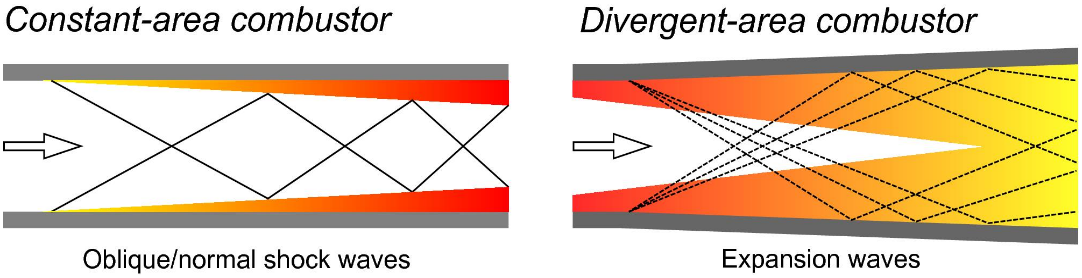

Figure 41. Schematics of combustion in (a) constant-area and (b) diverging combustors

In our previous study of combustion-induced choking in axisymmetric constant-area combustor (**Figure 41**a), the heat flux measurements at the combustor exit revealed a negligible contribution of combustion heating to the stagnation enthalpy of the supersonic core, and the entropy increase of supersonic core flow along the flowpath is contributed mostly by the total pressure loss originating from viscosity and shocklets in boundary regions with combustion heat addition. In this study, the combustor has a diverging angle to accommodate the potential flow separation and boundary layer development, and to alleviate the generation of oblique and/or normal shockwaves. Additionally, the shock reflections can be mitigated by the combustor area relief. The totality of effects from the diverging combustor leads to a supersonic combustor with enhanced combustion heat addition and improved performance (**Figure 41**b).

Figure 42 shows the typical scramjet operation mode transition from the dual-mode scram to the ram mode, which corresponding to the descending phase of hypersonic flight. The pressure measurements are conducted in the model scramjet with a 2-deg diverging combustor. The scramjet transition can be divided into three phases, i.e., the flame propagation phase, ram-mode phase and the unstart phase. In a typical test, the fuel is injected at the time of 0.26 s and the fuel mass flow reaches to its maximum and steady condition at 0.33 s. With the increasing of ethylene fueling rate below the choking limit, the combustion stabilizes inside the diverging combustor as indicated by the high-pressure region in the pressure contour. Pseudo shocks develop once the flow is choked by excessive heat release and the unsteady shockwaves propagate upstream until the cavity flameholder region. The flame and shock propagation in this phase are highly unstable. Once the flame propagates into the cavity, the strong combustion and flow blockage introduce back pressure that is sufficient high to separate the flow inside the isolator, as indicated by the high-pressure region in the pressure contour upstream of the cavity zone. The isolator is sufficient long to accommodate the pseudo shocks only during the 0.32-0.36 s. Around the 0.36 s, the pseudo shock is close to the scramjet inlet and the unsteady boundary layer separation starts to interact with the inlet. The unsteady flow dynamics drive the pseudo shock further upstream until a bow shock develops upstream of the inlet, which is called scramjet unstart. Once this bow shock develops, the flow compressed by the shock is spilled and the incoming mass flow rate is decreased. The combustion may exist inside the isolator region due to the reverse flow during an unstart event. As the incoming oxygen mass flow rate is decreased and the fuel mass flow rate is constant, the combustion intensity decreases at this time frame and results in lower flow blockage and weaker back pressure rise. The standing normal shock will be swallowed by the inlet and the air mass flow rate entering the scramjet engine increases. The combustion will recover due to the increased oxygen supply upstream. Once again, the increased combustion introduces strong heat release and choke the flow again. This entire process is cyclical, as indicated by the intense periodic oscillation over the entire internal flow channel of the scramjet model. Therefore, the flow oscillation is the totality of the scramjet inlet-isolator-combustor interactions. Further investigation on the flame dynamics during the unstart processes needs to be fully resolved and the strategy for unstart control needs to be proposed.

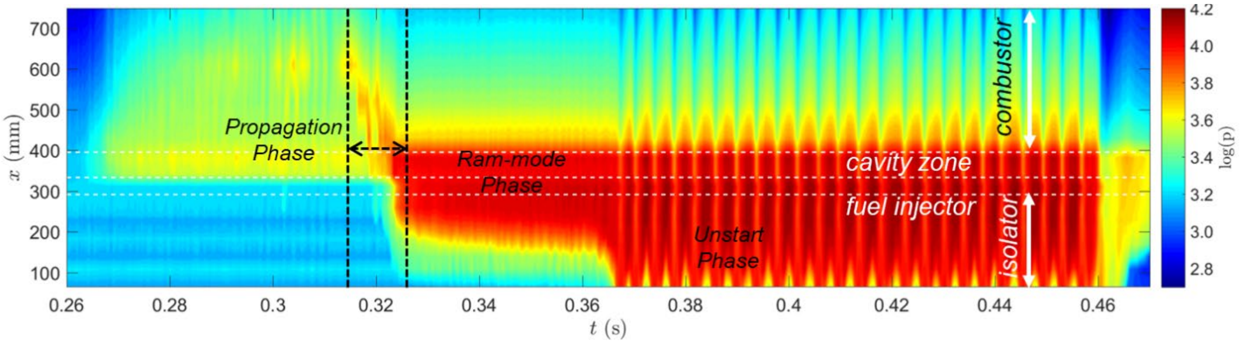

Figure 42. Pressure contour in the x-t plane during the scramjet dual-mode transition process.

8. CONCLUSION

Significant progress has been made in the experimental investigation of turbulent combustion in supersonic flows. These experiments were conducted in the unique arc-heated hypersonic wind tunnel ACT-II at the University of Illinois at Urbana-Champaign. The ACT-II facility has been developed and has proven to be an improved test bench for the turbulent combustion that occurs in scramjet engines, with a focus on the application of advanced laser diagnostic techniques.

The nano-LIBS was shown to be a practical and effective technique for quantitative gas property measurements in high-speed, reacting environments. Through the construction of an intensive spectrum database and the development of the direct spectrum matching procedure, fuel concentration and gas density were mapped throughout the flame holder cavity of a model scramjet operating at Mach 3 and with different geometries used to mimic the shock train formed in a practical combustor. In year IV, the introduction of fuel surrogates, like CO_2, allowed to better characterize fuel concentrations and statistics in non-combusting case. The use of a surrogate removed any limitation on the number of tests that can be performed but required the construction of an additional calibration table. Additionally, the improvements of the DSM calibration matrix through the increase in matrix density allow for reduced uncertainty at low local fuel mole fractions.

The highly efficient nature of the new CH C-X transition promises to enable both high speed and volumetric imaging of CH possible in turbulent combustion research. In collaboration with Dr. Campbell Carter at AFRL and with Dr. Jim Driscoll at the University of Michigan, we have demonstrated the capability of this strategy along with PIV in the Hi-Pilot combustor. A further improvement of the method was implemented to avoid the interference of scattered laser light with the resonance fluorescence at 314 nm. In the new approach CH radical was excited on a satellite transition at 310 nm and a sharp high-pass optical filter was used to remove the excitation wavelength from the collected signal. This technique allows simultaneous high-quality visualization of the CH fluorescence and PIV at high speed, as demonstrated in the Hi-Pilot combustor.

The experimental investigations in progress include the combustion-induced choking in an axisymmetric constant-area flow, the cavity flameholding in diverging combustors with various diverging cone angles, and the dynamics of the pseudo-shock in a scramjet isolator and on the instabilities leading to inlet unstart. The axisymmetric circular direct-connect combustor provides the combustion configuration that emphasizes the role played by the combustion-induced heat release and boundary layer in the initiation of shock train propagation. The diverging combustors provides area relief to accommodate the pressure rise, boundary layer development, flow separation and combustion heat release in the supersonic flow. The combustion phenomena occurring in the diverging combustor are different to that in the constant-area combustor with respect to the combustion heat addition into the core flow and the choking limit. The third study focuses its attention on the dynamics of the pseudo-shock in a scramjet isolator and on the instabilities leading to inlet unstart. In particular, the differences between combustion-induced and mass-induced unstart has been investigated in a circular geometry.

9. FUTURE PLANS

As this is the final report, the current project has ended as of 9/30/2019. The seeds of this project including the laser and optical diagnostics and most importantly the ACT-II facility will become the foundation for future studies in hypersonic propulsion systems.

10. COLLABORATIONS WITH AIR FORCE RESEARCH LABORATORY

As previously noted, much of the work discussed here was carried out in collaboration with the Propulsion Directorate at Wright Patterson Air Force Base. The Nano-Laser Induced Breakdown Spectroscopy (Nano-LIBS) measurements in particular were carried out in the TC-19 at WPAFB, and the results have been compared successfully to numerical simulations conducted by AFRL researchers.

11. PERSONNEL SUPPORTED

Faculty

Professor Tonghun Lee

Postdoctoral Scholars

Stephen Hammack (Staff member at AFRL)

Qili Liu

Graduate Students

Damiano Baccarella (Ph.D. student)

Brendan McGann (Ph.D. student)

Constandinos Mitsingas (Ph.D. student)

Gyu-Sub Lee (Ph.D. student)

12. PUBLICATIONS

Following publications have been published and/or submitted with support from this grant in these four years of the project.

Refereed Journals

1. Q. Liu, D. Baccarella, T. Lee, *Progress of Combustion Stabilization for Hypersonic Propulsion,* Progress in Aerospace Sciences, submitted at Oct. 2019.
2. D. Baccarella, G. Lee, Q. Liu, G. Elliot, J. Freund, T. Lee, *Laser-Induced Plasma Ignition Experiments in a Direct-Connect Supersonic Combustor at Mach 3,* Journal of Propulsion and Power, submitted at Oct. 2019.
3. Q. Liu, D. Baccarella, B. McGann, T. Lee, *Dual-Mode Operation and Transition in Axisymmetric Scramjets,* AIAA Journal, Article in Advance, 2019.
4. D. Baccarella, Q. Liu, B. McGann, T. Lee, *Combustion Induced Choking in an Axisymmetric Constant-Area Supersonic Flow*, AIAA Journal, Article in Advance, 2019.
5. Q. Liu, D. Baccarella, B. McGann, T. Lee, *Cavity-enhanced Combustion Stability in an Axisymmetric Scramjet Model,* AIAA Journal, 57, 9, 3898-3909, 2019.
6. Q. Liu, D. Baccarella, W. Landsberg, A. Veeraragavan, T. Lee, *Cavity Flameholding in an Optical Axisymmetric Scramjet in Mach 4.5 Flows,* Proceedings of Combustion Symposium, 37, 3, 3733-3740, 2019.
7. B. McGann, T. Lee, T. Ombrello, C.D. Carter, S.D. Hammack, H. Do, *Inlet Distortion Effects on Fuel Distribution and Ignition in Scramjet Cavity Flameholder,* Journal of Propulsion and Power, 35, 3, 601-613, 2019.
8. A. Skiba, C. Carter, S. Hammack, T. Lee, *A Simplified Approach to Simultaneous multi-scalar imaging in turbulent flames*, Combustion and Flame, 189, 207-211.
9. S. Hammack, C. Carter, A. Skiba, C. Fugger, J. Felvor, J. Miller, J. Gord, and T. Lee, *20 kHz* CH_2O *and OH PLIF with Stereo PIV*, Optics Letter, 43, 5, 1115-1118.
10. B. McGann, C. Carter, T. Ombrello, S. Hammack, T. Lee, H. Do, *Gas Property Measurements in a Supersonic Combustor using Nanosecond Gated Laser-Induced Breakdown Spectroscopy with Direct Spectrum Matching,* Proc. Comb. Symp. 36, 2, 2857-2864, 2017
11. Q. Liu, D. Baccarella, T. Lee, C. Carter and H. Do, *Influences of Inlet Geometry Modification on Scramjet Flow and Flame Dynamics*, Journal of Propulsion and Power, 33, 5, 1179-1186, 2016
12. Q. Liu, D. Baccarella, S. Hammack, T. Lee, C. Carter, H. Do., *Influence of Freestream Turbulence on Flame Dynamics in a Supersonic Combustor*, AIAA J., 55, 3, 913-918, 2016

13. N. Traina, T. Lee, J. Yoo, *Simultaneous diagnostics of simple hydrocarbon species in minute concentrations using supercontinuum laser absorption spectroscopy*, Applied Spectroscopy, submitted (2016)
14. D. Baccarella, Q. Liu, A. Passaro, T. Lee, H. Do, *Development of testing of the ACT-1 experimental facility for hypersonic combustion research*, Measurement Science and Technology, 27, 4 (2016)
15. B. McGann, C. Carter, T. Ombrello, S. Hammack, T. Lee, H. Do, *Direct Spectrum Matching of laser-induced breakdown for concentration and gas density measurements in turbulent reacting flows,* Combustion and Flame 162, 12, 4479-4485, 2015
16. L. Ma, Y. Wu, W. Xu, S. Hammack, T. Lee, C. Carter, Comparison of 2D and 3D flame topography measured by PLIF and tomographic chemiluminescence, Applied Optics, 55, 20, 5310-5315 (2016)
17. A. Skiba, T. Wabel, C. Carter, S. Hammack, J. Temme, T. Lee, J. Driscoll, *Reaction layer visualization: a comparison of two PLIF techniques and advantages of kHz imaging*, Proc. Comb. Symp. 36, 3, 4593-4601, 2017
18. C. Carter, S. Hammack, T. Lee, *High-Speed Flamefront Imaging in Premixed Turbulent Flames using Planar Laser-Induced Fluorescence of the CH C-X Band*, Combustion and Flame, 168, 66-74 (2016)
19. C.M. Mitsingas, R. Rajasegar, S. Hammack, H. Do, T. Lee, *High energy efficiency plasma conversion of CO_2 at atmospheric pressure using a direct coupled microwave plasma system*, IEEE Transactions on Plasma Science, 44, 4, 651-656 (2016)
20. J. Yoo, N. Traina, M. Halloran, T. Lee, *Minute concentration measurements of simple hydrocarbon species using supercontinuum laser absorption spectroscopy*, Applied Spectroscopy, 70, 6, 1063-1071 (2016)
21. C. Carter, S. Hammack, T. Lee, *High-Speed Planar Laser-Induced Fluorescence of the CH*
22. S. Hammack, C. Carter, T. Lee, *Continuous OH Planar Laser Imaging at 50 kHz Repetition Rate*, Applied Optics, 53, 23, 5246-5251 (2014)

Conference Proceedings

1. D. Baccarella, G. Lee, Q. Liu, G. Elliot, J. Freund, T. Lee, *Laser-Induced Plasma Ignition Experiments in a Direct-Connect Supersonic Combustor at Mach 3*, AIAA Propulsion and Energy 2019 Forum, Indianopolis, Indiana, 2019.
2. Q. Liu, D. Baccarella, T. Lee, *Combustion Stabilization in an Axisymmetric Scramjet in Mach 4.5 Flows*, AIAA Scitech 2019 Forum, San Diego, California, 2019.
3. B. McGann, T. Lee, T. Ombrello, C. D. Carter, S. Hammack, H. Do, *Statistical Measurements of Fuel Mole Fraction in Scramjet Cavity Flameholder with a Fuel Surrogate*, AIAA Scitech 2019 Forum, San Diego, California, 2019.
4. G. Lee, Q. Liu, D. Baccarella, G. Elliot, T. Lee, *A Novel Supersonic Injection Scheme for Laser Induced Breakdown Ignition*, 2018 Aerodynamic Measurement Technology and Ground Testing Conference, Atlanta, Georgia, 2018.
5. Q. Liu, D. Baccarella, B. McGann, T. Lee, and H. Do, *Experimental Investigation of Single Jet and Dual Jet Injection in a Supersonic Combustor*, 2018 AIAA Aerospace Meeting, Kissimmee, Florida, 2018.
6. D. Baccarella, Q. Liu, B. McGann, T. Lee, and H. Do, Experimental Study of Heat Release Induced Choking in a Supersonic Circular Combustor, 2018 AIAA Aerospace Meeting, Kissimmee, Florida, 2018.

7. A. Skiba, C. Carter, S. Hammack, T. Lee, *A Simplified Approach to Multi-Scalar Imaging to Turbulent Premixed Flames*, 10th U.S. National Combustion Meeting, College Park, Maryland, 2017
8. D. Baccarella, Q. Liu, T. Lee, *The Supersonic Combustion Facility ACT-2*, AIAA SciTech, AIAA-2017-0103, 2017
9. Q. Liu, D. Baccarella, T. Lee, C. Carter, H. Do, *Three-Dimensional Visualization of Flow and Flame in a Model Scramjet in Mach 4.5 Flows*, AIAA SciTech, AIAA-2017-0341, 2017
10. T. Ombrello, E. Hassan, C. Carter, B. McGann, T. Lee, H. Do, D. Peterson, P. Ivancic, E. Luke, *Establishing the Controlling Parameters of Ignition in High-Speed Flow*, AIAA Scitech 2016

13. REFERENCES

[x] W. H. Heiser, and D. T. Pratt, Hypersonic Airbreathing Propulsion (AIAA Education Series, 1994).

[x] E. T. Curran, and S. N. B. Murthy, Scramjet Propulsion (AIAA, Progress in Astronautics and Aeronautics, 2000).

[x] J. Li, F. Ma, V. Yang, K. C. Lin, and T. A. Jackson, "A Comprehensive Study of Combustion Oscillations in a Hydrocarbon-Fueled Scramjet Engine," 45th AIAA Aerospace Sciences Meeting and Exhibit, AIAA 2077-2836 (2007).

[x] F. Fuest, M. J. Papageorge, W. R. Lempert, and J. A. Sutton, "Ultrahigh laser pulse energy and power generation at 10 kHz," Optics letters 37, 3231-3233 (2012).

[x] K. Gabet, R. Patton, N. Jiang, W. Lempert, and J. Sutton, "High-speed CH2O PLIF imaging in turbulent flames using a pulse-burst laser system," Appl. Phys. B 106, 569-575 (2012).

[x] M. N. Slipchenko, J. D. Miller, S. Roy, J. R. Gord, S. A. Danczyk, and T. R. Meyer, "Quasi-continuous burst-mode laser for high-speed planar imaging," Optics letters 37, 1346-1348 (2012).

[x] S. Hammack, C. Carter, C. Wuensche, and T. Lee, "Continuous OH Planar Laser Imaging at 50 kHz Repetition Rate," Appl. Opt. 53, 5246-5251 (2014).

[x] C. Carter, S. Hammack, and T. Lee, "High-speed planar laser-induced fluorescence of the CH radical using the C2Σ+−X2Π(0,0) band," Appl. Phys. B 116, 515-519 (2014).

[x] E. Pfender, "Electric arcs and arc gas heaters," Gaseous electronics 1, 291-298 (1978).

[x] C. T. Bowman, "Kinetics of pollutant formation and destruction in combustion," Progress in energy and combustion science 1, 33-45 (1975).

[x] P. Guo, and Z. Chen, "Ignition enhancement of ethylene/air by NOx addition," Chinese Journal of Aeronautics 26, 876-883 (2013).

[x] K. Sutton, and R. A. Graves, " A general stagnation-point convective-heating equation for arbitrary gas mixtures," NASA TR R-376, 1971.

[x] H. A. Stein, and W. R. Watson, "The theoretical enthalpy distribution of air in steady flow along the axis of a direct-current electric arc," NASA TN D-1331, 1962.

[x] A. W. Miziolek, V. Palleschi, and I. Schechter, Laser induced breakdown spectroscopy (Cambridge University Press, 2006).

[x] S. Musazzi, and U. Perini, "Laser-Induced Breakdown Spectroscopy," Laser-Induced Breakdown Spectroscopy: Theory and Applications, Springer Series in Optical Sciences, Volume 182. ISBN 978-3-642-45084-6. Springer-Verlag Berlin Heidelberg, 2014 1 (2014).

[x] N. Reinhard, "Laser-Induced Breakdown Spectroscopy: Fundamentals and Applications," (Germany: Springer, 2012).

[x] L. G. Blevins, C. R. Shaddix, S. M. Sickafoose, and P. M. Walsh, "Laser-induced breakdown spectroscopy at high temperatures in industrial boilers and furnaces," Applied optics 42, 6107-6118 (2003).

[x] H. Do, and C. Carter, "Hydrocarbon fuel concentration measurement in reacting flows using short-gated emission spectra of laser induced plasma," Combustion and Flame 160, 601-609 (2013).

[x] H. Do, C. Carter, Q. Liu, T. Ombrello, S. Hammack, T. Lee, and K.-Y. Hsu, "Simultaneous density and fuel concentration measurement in a supersonic combustor using laser induced breakdown," Proceedings of Combustion Institute 35, 2155–2162 (2015).

[x] F. Ferioli, and S. G. Buckley, "Measurements of hydrocarbons using laser-induced breakdown spectroscopy," Combustion and Flame 144, 435-447 (2006).

[x] V. Sturm, and R. Noll, "Laser-induced breakdown spectroscopy of gas mixtures of air, CO 2, N 2, and C 3 H 8 for simultaneous C, H, O, and N measurement," Applied optics 42, 6221-6225 (2003).

[x] M. Brewczyk, "The role of electrons in laser-induced explosion of diatomic molecules and small clusters," Laser Physics 8, 124-128 (1998).

[x] D. A. Cremers, F. Y. Yueh, J. P. Singh, and H. Zhang, Laser - Induced Breakdown Spectroscopy, Elemental Analysis (Wiley Online Library, 2006).

[x] S. Yalcin, D. Crosley, G. Smith, and G. W. Faris, "Influence of ambient conditions on the laser air spark," Applied Physics B: Lasers and Optics 68, 121-130 (1999).

[x] M. S. Chou, and A. M. Dean, "Excimer laser perturbations of methane flames: High temperature reactions of OH and CH," International journal of chemical kinetics 17, 1103-1118 (1985).

[x] J. B. Jeffries, R. A. Copeland, and D. R. Crosley, "Transition probabilities in the $C^2\sum^+$-X^2II system of CH," Journal of Quantitative Spectroscopy and Radiative Transfer 37, 419-423 (1987).

[x] A. Hirano, M. Ippommastu, and M. Tsujishita, "Two-dimensional digital imaging of the CH distribution in a natural gas/oxygen flame at atmospheric pressure and detection of A-state emission by means of C-state excitation," Optics letters 17, 303-304 (1992).

[x] C. D. Carter, J. M. Donbar, and J. F. Driscoll, "Simultaneous CH planar laser induced fluorescence and particle imaging velocimetry in turbulent nonpremixed flames," Appl. Phys. B 66, 129-132 (1998).

[x] J. Luque, J. B. Jeffries, G. P. Smith, D. R. Crosley, K. T. Walsh, M. B. Long, and M. D. Smooke, "CH (A-X) and OH (A-X) optical emission in an axisymmetric laminar diffusion flame," Combustion and Flame 122, 172-175 (2000).

[x] W. Ubachs, G. Meyer, J. Ter Meulen, and A. Dymanus, "Hyperfine structure and lifetime of the C 2Σ+, v= 0 state of CH," The Journal of chemical physics 84, 3032-3041 (1986).

[x] J. Luque, and D. R. Crosley, "LIFBASE: Database and spectral simulation for diatomic molecules," SRI International, MP-99-0099 (2005).

[x] M. J. Bulman, and A. Siebenhaar, "The Rebirth of Round Hypersonic Propulsion, " 42ed AIAA/ASME/SAE/ASEE Joint Propulsion Conference and Exhibit, AIAA Paper 2006-5035, July 2006.

[x] F. S. Billig, and A. P. Kothari, "Streamline Tracing: Technique for Designing Hypersonic Vehicles," Journal of Propulsion and Power, Vol. 16, No. 3, 2000, pp. 465-471.

[x] M. K. Smart, and C. A. Trexler, "Mach 4 Performance of Hypersonic Inlet with Rectangular-to-elliptic Shape Transition," Journal of Propulsion and Power, Vol. 20, No. 2, 2004, pp. 288-293.

[x] K. Matsuo, Y. Miyazato, and H. Kim, "Shock Train and Pseudo-Shock Phenomena in Internal Gas Flows," Progress in Aerospace Sciences, 35, 33-100 (1999).

[x] W. H. Heiser, and D. T. Pratt, Hypersonic Airbreathing Propulsion (AIAA Education Series, 1994).

[x] C. Segal, The Scramjet Engine: Processes and Characteristics, Cambridge Aerospace Series, Cambridge University Press, 2009.

[x] M. R. Gruber, R. A. Baurle, T. Mathur, and K, Hsu, "Fundamental Studies of Cavity-Based Flameholder Concepts for Supersonic Combustors", Journal of Propulsionand Power, 17, 146-153 (2001).

[x] A. Ben-Yakar, and R.K. Hanson, "Cavity Flame-Holders for Ignition and Flame Stabilization in Scramjets: An Overview", Journal of Propulsionand Power, 17, 869-877 (2001).

[x] T. Mathur, M. Gruber, K. Jackson, J. Donbar, W. Donaldson, T. Jackson, and F. Billig, "Supersonic Combusiton Experiments with a Cavity-Based Fuel Injector", Journal of Propulsionand Power, 17, 1305-1312 (2001).

[x] C. C. Rasmussen, J. F. Driscoll, K. Hsu, J. Donbar, M. Gruber, and C. Carter, "Stability Limits of Cavity-Stabilized Flames in Supersonic Flow", Proceedings of the Combustion Institute, 30, 2825-2833 (2005).

[x] Y. Tian, S. Yang, J. Le, F. Zhong, and X. Tian, "Investigation of Cmobustion Process of a Kerosene Fueled Combustor with Air Throttling", Combustion and Flmame 179, 74-85 (2017).

[x] E. Jeong, I. Jeung, S. O'Byrne, and A. Houwing, "Investigation of Supersoinc Combustion with Angled Injection in a Cavity-Based Combustor", Journal of Propulsionand Power, **24**, 1258-1268 (2008).

[x] R. Yentsch, and D. Gaitonde, "Comparison of Mode-Transition Phenomena in Axisymmetric and Rectangular Scramjet Flowpaths", 52ed Aerospace Sciences Meeting, National Harbor, Maryland (2014).

[x] M.K. Smart, and C.A. Trexler, "Mach 4 Performance of Hypersonic Inlet with Rectangular-to-Elliptical Shape Transition", Journal of Propulsionand Power, 20, 288-293 (2004).

[x] Z. Denman, W. Chan, S. Brieschenk, A. Veeraragavan, V. Wheatly, and M. Smart, "Ignition Experiments of Hydrocarbons in a Mach 8 Shape-Transitioning Scramjet Engine," Journal of Propulsionand Power, 32, 1462-1471 (2016).

[x] Z. Denman, V. Wheatly, M. Smart, and A. Veeraragavan, "Supersonic Combusiton of Hydrocarbons in a Shape-Transitioning Hypersoinc Engine," Proceedings of the Combustion Institute, 36, 2883-2891 (2017).

[x] M. Gruber, S. Smith, and T. Mathur, "Experimental Characterization of Hydrocarbon-fueled Axisymmetric Scramjet Combustor Flowpaths," 17th AIAA International Space Planes and Hypersonic Systems and Technologies Conference, San Francisco, California (2011).

[x] F.S. Billig, "Design of Supersonic Comubstors Based on Pressure-Area Fields," Symposium (International) on Combustion, 11, 755-769 (1967).

[x] D. Riggins, R. Tackett, and T. Taylor, "Thermodynamic Analysis of Dual-Mode Scramjet Engine Operation and Performance," 14th AIAA/AHI Space Planes and Hypersonic Systems and Technologies Conference (2006).

[x] W. Yao, Y. Yuan, X. Li, J. Wang, K. Wu, X. Fan, "Comparative Study of Elliptic and Round Scramjet Combustors Fueled by RP-3," Journal of Propulsion and Power, 34, 772-786 (2018).